

# Nearby galaxies in the LOFAR Two-metre Sky Survey

## IV. A fundamental plane of the radio–SFR relation

V. Heesen<sup>1</sup>, H. W. Edler<sup>2</sup>, M. Brüggen<sup>1</sup>, M. Stein<sup>3</sup>, D. J. Bomans<sup>3</sup>, R. Paladino<sup>4,5</sup>, K. T. Chyży<sup>6</sup>, K. Małek<sup>7,8</sup>,  
M. A. Lara-López<sup>9,10</sup>, and F. S. Tabatabaei<sup>11</sup>

<sup>1</sup> Hamburger Sternwarte, University of Hamburg, Gojenbergsweg 112, 21029 Hamburg, Germany  
e-mail: volker.heesen@uni-hamburg.de

<sup>2</sup> ASTRON, the Netherlands Institute for Radio Astronomy, Postbus 2, NL-7990 AA Dwingeloo, The Netherlands

<sup>3</sup> Ruhr University Bochum, Faculty of Physics and Astronomy, Astronomical Institute (AIRUB), 44780 Bochum, Germany

<sup>4</sup> European Southern Observatory, Karl-Schwarzschild-Strasse 2, 85748 Garching, Germany

<sup>5</sup> INAF-Istituto di Radioastronomia, Via P. Gobetti 101, 40129 Bologna, Italy

<sup>6</sup> Astronomical Observatory of the Jagiellonian University, ul. Orla 171, 30-244 Kraków, Poland

<sup>7</sup> National Centre for Nuclear Research, Pasteura 7, 02-093, Warsaw, Poland

<sup>8</sup> Aix-Marseille Université, CNRS, CNES, LAM, Marseille, France

<sup>9</sup> Departamento de Física de la Tierra Astrofísica. Universidad Complutense de Madrid (UCM), E-28040 Madrid, Spain

<sup>10</sup> Instituto de Física de Partículas y del Cosmos, IPARCOS, Fac. C.C. Físicas, Universidad Complutense de Madrid, E-28040 Madrid, Spain

<sup>11</sup> School of Astronomy, Institute for Research in Fundamental Sciences (IPM), P.O. Box 1956836613, Tehran, Iran

Received date / Accepted date

### ABSTRACT

*Context.* Radio continuum emission has the potential to be an extinction-free tracer of star formation. However, the relation between radio continuum luminosity and star formation rate, the radio-SFR relation, is potentially limited by various effects such as cosmic-ray transport, free-free absorption, and cosmic-ray electron energy losses.

*Aims.* We aim to calibrate the radio-SFR relation in a sample of nearby galaxies ranging from dwarf to spiral galaxies covering nearly five orders of magnitude in SFR range. We include, both, global (individual galaxies) and local (spatially resolved, kiloparsec sized) measurements.

*Methods.* We measured radio continuum luminosities at 144 MHz using observations with the LOw Frequency ARray (LOFAR) and measure radio spectral indices using ancillary 1.4 GHz data. Selecting 70 nearby (distance  $d < 30$  Mpc) galaxies, 15 of which were used for local measurements, with rich ancillary data we present a study of the radio-SFR relation using total infrared, mid-infrared,  $H\alpha$ , and far-ultraviolet as complementary SFR tracers. About one third of our sample are at least moderately star-forming edge-on galaxies with the remaining ones chosen to be a representative sample of a wide range of morphological types and SFR values.

*Results.* For the first time, we show that the radio luminosity ( $L_{144}$ ), the star-formation rate (SFR), and the radio spectral index ( $\alpha$ ) define a ‘fundamental plane’ in the  $[\log(L_{144}), \log(\text{SFR}), \alpha]$  space. This allows us to define a unified radio-SFR relation that works both for global and local data when using the radio spectral index as a second parameter.

*Conclusions.* A unified radio-SFR relation for, both, global and local data may serve as a litmus test for galaxy simulations that include the effect of cosmic rays and magnetic fields. It also strengthens the case for using the radio-SFR relation as an extinction-free tracer of star formation.

**Key words.** cosmic rays – galaxies: magnetic fields – galaxies: fundamental parameters – galaxies: star formation – radio continuum: galaxies

## 1. Introduction

The star-formation rate (SFR) is one of the fundamental parameters to probe galaxy formation and evolution. Hence, considerable effort has gone into the calibration of various star formation tracers across the electromagnetic spectrum using, both, line and continuum emission (Kennicutt & Evans 2012). Radio continuum is one of those tracers (Murphy et al. 2011), and it offers us some unique benefits such as high angular resolution using interferometric observations, extinction-free star formation measurements, ground-based observations, and wide-field survey capabilities. Also, radio continuum is one of the few avenues to study both cosmic rays and magnetic fields in galaxies, some of the crucial ingredients for state-of-the-art galaxy

evolution models (Thompson & Heckman 2024). Recent developments in high-performance computing made it possible to conduct all-sky surveys with radio interferometers at high angular resolution and good sensitivity such as the Evolutionary map of the Universe (EMU; Norris et al. 2021) survey with the Australian Square Kilometre Array Pathfinder (ASKAP) and the LOFAR Two-metre Sky Survey (Shimwell et al. 2017, 2019) and Shimwell et al. (2026) with the LOw Frequency ARray (LOFAR; van Haarlem et al. 2013).

Analysis of the LOFAR data has shown that galaxies follow a close relation between radio continuum luminosity and SFR, the radio-SFR relation in short (e.g. Gürkan et al. 2018). At these low frequencies the relation is significantly affected not

just by the SFR but also by the mass: galaxies that are more massive, are also brighter in the radio continuum compared to their SFR (Smith et al. 2021; Shenoy et al. 2026). One possible explanation is that more massive galaxies are better cosmic-ray electron (CRE) calorimeters and thus have steeper radio continuum spectra (Heesen et al. 2022; Edler et al. 2024). There are several processes that shape the radio continuum spectra such as free-free absorption and cosmic-ray ionisation losses that suppress the emission at low frequencies and thus flatten the spectrum (Basu et al. 2015). On the other hand, synchrotron and inverse Compton radiation losses steepen the radio continuum spectrum. Hence, there is a complex interplay with cosmic-ray ageing, transport, and acceleration that governs the details of the radio-SFR relation (Roth et al. 2023).

These processes can explain why the relation is strongly super-linear for global measurements (e.g. Bell 2003; Li et al. 2016; Heesen et al. 2022), while it is strongly sub-linear for local measurements (e.g. Basu et al. 2012; Heesen et al. 2024). In order to improve the radio-SFR calibration, it was shown in earlier work that restricting the analysis to areas near star formation sites can reduce the scatter significantly (Dumas et al. 2011; Basu et al. 2012). In later work it was shown that the radio spectral index can be a good proxy for these areas and selecting only data in agreement with the CRE injection spectrum (Heesen et al. 2014, 2019). As an extension to these papers it was shown that taking into account the radio continuum spectrum, the radio-SFR relation can be linearised using the radio spectral index as an additional information (Heesen et al. 2024) or using more than one frequency (Tabatabaei et al. 2017). One aspect that is particularly exciting is the prospect of a unified radio-SFR relation that holds, both, at global and local i.e. kiloparsec scales (Heesen et al. 2024).

This empirical calibration showed a strong relation between the relative radio brightness, i.e. the ratio of radio intensity to SFR surface density, as function of radio spectral index (Heesen et al. 2024). It was also shown that this relation can be applied to global measurements in order to approximately linearise the radio-SFR relation. Qualitatively this can be understood as a superposition of processes that flatten the spectrum and thus suppress radio continuum emission at low frequencies, such as cosmic-ray ionisation losses and free-free absorption. On the other hand synchrotron radiation losses steepen the spectrum and result in radio-bright galaxies (Lacki et al. 2010). Processes that flatten the spectrum have been observed in nearby starburst galaxies where they affect the global spectrum (Adebahr et al. 2013; Kapińska et al. 2017) or in spatially resolved observations of nearby galaxies (Gajović et al. 2024, 2025). Simulations indicate that galaxies might be good electron calorimeters and a low-frequency flattening stems from free-free absorption (Werhahn et al. 2021).

In this work we wish to explore the low-frequency radio-SFR relation both on a global and local (kiloparsec sized) basis. We use images from the third data release of LoTSS (LoTSS-DR3; Shimwell et al. 2026) to probe galaxies from low-mass dwarf galaxies to massive spiral galaxies. We then relate the ratio of radio to ancillary SFR surface brightness to the radio spectral index and show that the global and local data indeed follow the same trend. This potentially allows us to define a unique radio-SFR relation where the radio spectral index is used as a second parameter. This work albeit only expanding the sample of LoTSS-DR2 (Heesen et al. 2022) by about 50 per cent, extends the mass and SFR range to now four orders of magnitude (previously less than three orders of magnitude). Extending our previous work in Heesen et al. (2024) where we analysed the local measure-

ments we now expand this work to a consistent description of both global and local data making this distinction obsolete.

This paper is organised as follows: Section 2 describes our sample selection, data reduction, and methodology. In Sect. 3 we present our resulting radio-SFR relations and radio spectral indices that we relate to fundamental galaxy parameters. We discuss our results in Sect. 4 before we conclude in Sect. 5. Appendix A contains our presented observational results.

## 2. Data and methodology

### 2.1. Galaxy sample

We defined our galaxy sample in Heesen et al. (2022). In brief, we draw them from the SIRTf Nearby Galaxies Survey (SINGS; Kennicutt et al. 2003), Key Insights on Nearby Galaxies: A Far-Infrared Survey with Herschel: Survey Description and Image Atlas (KINGFISH; Kennicutt et al. 2011) and Continuum Halos in nearby galaxies: An EVLA survey (CHANG-ES; Irwin et al. 2012, 2024). The three galaxies which are only in KINGFISH but not in SINGS are NGC 2146, IC 342, and NGC 5457. Finally, we added another four galaxies, namely IC 10, NGC 598 (M33), NGC 4214, and NGC 4449. Three of these are star-burst dwarf irregular galaxies and M33 is the most nearby galaxy, which we can easily image as it is less than  $1^\circ$  in apparent size. The SINGS and Kingfish samples contain nearby galaxies (distance  $d < 30$  Mpc), and are chosen in such a way that they are representative in morphological type, infrared luminosity (proxy for SFR) and far-infrared-to-optical luminosity ratio (proxy for specific SFR). The CHANG-ES galaxies are chosen as edge-on galaxies (inclination angle  $i > 75^\circ$ ), with an optical size between 4 and  $15'$  and a radio flux density of  $>23$  mJy at 1.4 GHz.

In total, the sample contains 76 galaxies, 45 of which we published already in Heesen et al. (2022) based on LoTSS-DR2 data. With LoTSS-DR3, we were able to increase the sample size and so to include a number of low-mass dwarf galaxies which extends our sample to galaxies with only little star formation. Of the 76 galaxies, we found 70 galaxies suitable for our analysis. We left out six galaxies, namely M81 DwA, Ho IX, NGC 3190, NGC 4536, DDO 154, and DDO 165. The dwarf galaxies M81 DwA, Ho IX, DDO 154, and DDO 165 were non-detections. We searched at their position for a  $2\sigma$  detection in the  $20''$  maps with no detection. We discarded in those cases point-like sources at  $6''$ , likely background galaxies. These were checked with Pan-STARRS (Panoramic Survey Telescope and Rapid Response System; Chambers et al. 2016) optical overlays. NGC 3190 is contaminated by a background source, a Fanaroff–Riley type 2 radio galaxy. NGC 4536 was left out as the image quality was far inferior compared with the other data. This is probably caused by a combination of low declination and proximity to Virgo A.

We present our data in these four different sub-groups of CHANG-ES (21), SINGS (42), Kingfish+ (three), and ‘Extra’ (four) galaxies. These individual galaxies are referred to as ‘global’ data in what follows. We complement the global data with spatially resolved data. For this we use the galaxy sample as presented in Heesen et al. (2024). These include 15 galaxies from the SINGS sample. For these galaxies a spatial resolution of approximately one kiloparsec is reached. These measurements are referred to as ‘local’ data.

### 2.2. LOFAR data

We use data from the third data release of the LOFAR Two-metre Sky Survey (LoTSS-DR3; Shimwell et al. 2026) in conjunc-

tion with previously analysed data from the second data release (Heesen et al. 2022; Shimwell et al. 2022). We use the maps with 20'' angular resolution; alternatively, there are also maps at 6'' angular resolution.<sup>1</sup> For some galaxies (NGC 4254, 4321, and 4450) that are in the vicinity of Virgo A (M 87), we used data from the ‘Virgo Cluster multi-Telescope Observations in Radio of Interacting galaxies and AGN’ project (VICTORIA; Edler et al. 2023). These data are taken in an identical setup to LoTSS but are especially calibrated and imaged maps that can deal with the high-dynamic range required. The map of IC 10 was obtained from Heesen et al. (2018) and has a lower angular resolution of 44''. We then defined elliptical contours based on the optical centre (obtained from the NASA Extragalactic Data Base) and position angle (see Appendix A) such that they approximately enclose the the  $3\sigma$  contours of the 144 MHz radio continuum map. The intensity is then integrated within these elliptical regions to obtain the flux density. In a few cases (NGC 4236 and 4254) we subtracted the flux density of unrelated background sources, but in most cases they could be neglected within the uncertainties.

The radio flux densities were converted into radio luminosities without  $k$ -correction, meaning we assume that the rest frequency is equivalent to the observed frequency. As the redshift of our sample galaxies is  $< 0.01$ , this is a good approximation. Hence, we obtain for the radio continuum luminosity at 144 MHz:

$$L_{144} = 4\pi d^2 S_\nu, \quad (1)$$

where  $S_\nu$  is the integrated flux density at 144 MHz and  $d$  is the distance.

### 2.3. Star formation rates

The SFRs were calculated in two different ways (see also Appendix A.1). First, for global data we used a combination of  $H\alpha$  and mid-infrared observations to calculate dust-corrected  $H\alpha$  luminosities. Second, for the local data, we used a combination of mid-infrared and far-ultraviolet observations. While it would be preferable of course to have an entirely consistent approach, these two methods are consistent with each other to an accuracy of about 0.1 dex at SFR values  $> 10^{-3} M_\odot \text{ yr}^{-1}$ , where the bulk of our data points reside (Leroy et al. 2012). At lower SFRs, the uncertainties become larger of course. The limitation of our approach is that for galaxies at higher masses the mid-infrared emission becomes optically thick so that the SFRs are systematically too low (Vargas et al. 2019). The alternative is to use total infrared (TIR) luminosities to measure SFRs. However, at low masses, the TIR luminosities are too low since dwarf galaxies are dust deficient. In Appendix A.2 we show selected alternative results when using the TIR SFRs for the global data points. In Appendix A.3 we show a comparison of the different SFRs and further motivate our choice by showing that the global and local SFRs are indeed consistent with our approach.

Hence, for the global measurements, we used dust-corrected  $H\alpha$  luminosities. These were adopted from Kennicutt et al. (2011) based on the calibration presented in Kennicutt et al. (2009) and tabulated in Calzetti et al. (2010). The method combines  $H\alpha$  data with mid-infrared data at 24  $\mu\text{m}$ . For the CHANG-ES sample we simply used the SFRs from Wiegert et al. (2015). They are solely based on the 22  $\mu\text{m}$  fluxes with the *WISE* satellite. These are then converted using the relation presented in Jarrett et al. (2013) (see also Rieke et al. 2009). This assumes that

the mid-infrared emission captures all of the star-forming activity and that we do not need additional ultraviolet or  $H\alpha$  observations to estimate the SFR. Since the CHANG-ES galaxies are highly inclined thus at high optical depth, this should be a reasonable assumption. The more likely source of bias, affecting all our SFRs, is including ‘diffuse’ mid-infrared emission that reflects dust heated by an older stellar population (e.g. Belfiore et al. 2023). For any galaxies not in these samples, we used archival  $H\alpha$  and *Spitzer* 24  $\mu\text{m}$  data to calculate dust-corrected  $H\alpha$  luminosities. These are then converted into the SFRs using the conversion by Kennicutt et al. (2009).

For the local SFR measurements, we used the SFR surface density maps of Leroy et al. (2008) which are based on a combination of *GALEX* far-ultraviolet data at 156 nm and *Spitzer* 24  $\mu\text{m}$  data. These are excellent maps with good angular resolution of 13''.5 and very good sensitivity of  $< 10^{-4} M_\odot \text{ yr}^{-1} \text{ kpc}^{-2}$ .

### 2.4. Local data

In order to generate the local data, we used the software radio-pixel-plots (RPP).<sup>2</sup> For this we used radio continuum maps at 144 MHz from LOFAR and at 1365 MHz from the Westerbork Synthesis Radio Telescope (WSRT; Braun et al. 2007). We also used hybrid SFR surface density maps based on a combination of *GALEX* far-ultraviolet data at 156 nm and *Spitzer* 24  $\mu\text{m}$  data (Leroy et al. 2008).

To compare the global SFRs with those from spatially resolved measurements, we converted the radio intensities into luminosities. Basically, we convolved the maps with a Gaussian to an angular resolution where the full width at half maximum corresponds to a projected distance of 1.2 kpc (for some galaxies we chose slightly larger values). Then the maps were binned into pixel elements with 1.2 kpc side length. These values were then extracted using a  $3\sigma$  lower cutoff in radio continuum emission at 144 and 1365 MHz and in SFR surface density (see Heesen et al. 2024, for more details).<sup>3</sup> In order to calculate radio continuum luminosities we used:

$$L_{144} = 4\pi\Omega d^2 I_\nu, \quad (2)$$

where  $\Omega$  is the solid angle of the area  $A$  observed in the galaxy. Our maps were convolved to a Gaussian beam such that  $\Omega = 2\sqrt{2 \ln 2} \text{FWHM}^2$ , where FWHM is the full width at half maximum of the Gaussian beam. The FWHM is chosen such that the projected length in the galaxy is equivalent to 1.2 kpc.

The star formation rates were calculated with  $\text{SFR} = A\Sigma_{\text{SFR}}$ , where  $A = 1.2 \times 1.2 \text{ kpc}^2$  (in some cases the area is slightly larger). In total, there are 2119 local data points. In detail, NGC 628 (132 data points), NGC 925 (176), NGC 2403 (68), NGC 2841 (190), NGC 2903 (98), NGC 2976 (17), NGC 3184 (238), NGC 3198 (53), NGC 3938 (170), NGC 4254 (233), NGC 4725 (103), NGC 4736 (46), NGC 5055 (146), NGC 5194 and NGC 5195 (278), and NGC 7331 (171). Of course, we would expect that the sum of the local SFRs is similar to the global SFR for each galaxy for consistency. This is indeed at least approximately the case (see Appendix A.3). Small deviations are expected because the local data exclude small parts of the galaxies in particular galactic nuclei which may be influenced by an active galactic nucleus and some prominent background sources. These parts of the SFR maps were masked.

<sup>2</sup> <https://github.com/sebastian-schulz/radio-pixel-plots>

<sup>3</sup> Since the output of RPP is the radio SFR surface density converted according to Eq. (3) in Heesen et al. (2024), we first converted them back to intensities.

<sup>1</sup> <https://lofar-surveys.org>

## 2.5. Radio spectral indices

We obtained flux densities at around 1.4 GHz from the literature in order to calculate radio spectral indices. To this end we use mostly data at 1365 MHz from the Westerbork Synthesis Radio Telescope (WSRT; Braun et al. 2007) and data at 1570 MHz from the Jansky Very Large Array (JVLA; Wiegert et al. 2015). For those galaxies where they were not available we use other data from the literature such as from the 100 m Effelsberg telescope (Tabatabaei et al. 2017) and the Jansky Very Large Array (eg. Yun et al. 2001). Details can be found in Appendix A.4. Radio spectral indices are then calculated following the convention  $S_\nu \propto \nu^\alpha$ .

In a few cases (IC 2574 and DDO 53) instead of using the published flux densities, we re-measured the flux densities directly from the published maps using our own apertures. The reason is that our assumed apertures were very different from those in the literature. The reason is that the LOFAR maps show more extended emission, hence our integration regions were larger. In NGC 4236 and 4254 we measured the flux densities with our own regions and also subtracting background sources as we did for the LOFAR data.

## 2.6. Uncertainties, binning, and fitting of data

For the LOFAR data, we assumed an absolute flux-density scale uncertainty of 10%, following Shimwell et al. (2026); for the galaxies from the VICTORIA survey with LOFAR we assumed 20% uncertainty (Edler et al. 2023). For the global and local SFR measurements, we assume an uncertainty of 8%. This value should be considered as flux uncertainty only, assuming 15% uncertainty of either the H $\alpha$  (Kennicutt et al. 2009) or the far-ultraviolet flux (Gil de Paz et al. 2007) and 2% for the mid-infrared flux (Jarrett et al. 2013). This assumes that both are contributing about the same to the SFR (Leroy et al. 2012). We note that the actual calibration of SFRs even for global SFR measurements are about only 50% accurate at best; for local measurements the uncertainties are even larger (Leroy et al. 2012). Local measurements in the radio continuum may have also a larger uncertainty, in particular in areas of low signal-to-noise ratios. This we have attempted to mitigate using a  $3\sigma$  lower cut-off in radio continuum intensities, where  $\sigma$  the RMS noise value of the intensity map.

We binned our local data into twelve bins, separated by 0.25 dex in SFR values. For these we calculated the mean of the logarithmic radio luminosities and the mean of the logarithmic SFR values as well as the mean radio spectral index. For uncertainties we took the standard deviation of the mean. These data are referred to as ‘binned local data’. We fit our data to both global and binned local data, unless otherwise mentioned. This in effect applies a weighting to the fitting such that we prevent giving a lot of weight to the local measurements since there are so many more of them.

Best-fitting  $f(x)$  relations were obtained with the orthogonal distance regression (ODR) method. This method can take  $x$  uncertainties into account. In our case, this was done where  $x$  is either the SFR or the radio spectral index. For best-fitting  $f(x, y)$  bivariate relations with two variables we took only errors of the fitted values into account.

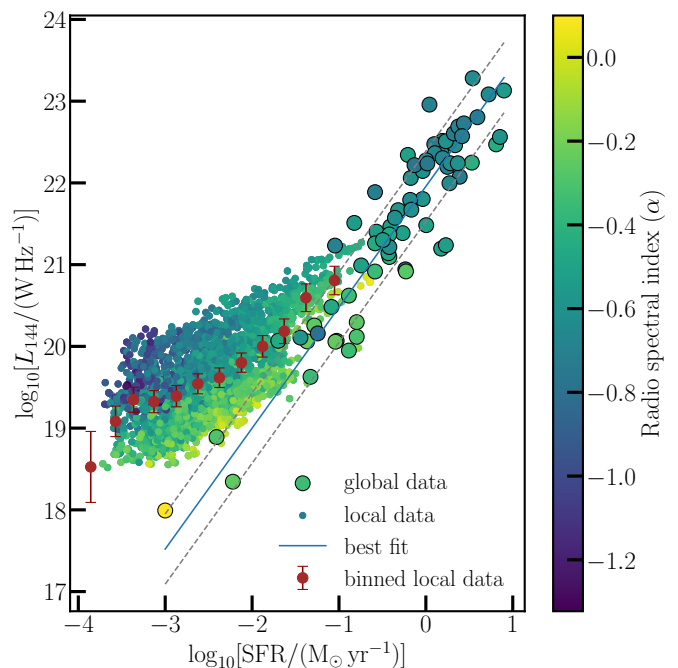


Fig. 1: Radio-SFR relation. Radio continuum luminosity at 144 MHz as a function of the SFR. Large data points show global and small data points local measurements (the latter largely overlapping). The best-fitting radio-SFR relation to the global data is shown as well (solid line with a  $\pm 1\sigma_y$  interval indicated by dashed lines). Red data points with error bars show binned local data. The SFR was derived from a combination of mid-infrared data with either H $\alpha$  (global) or far-ultraviolet (local data). Data points are coloured according to their radio spectral index between 144 MHz and approximately 1400 MHz.

## 3. Results

### 3.1. Radio-SFR relation

First, we investigate the global radio-SFR relation. For this we parametrise the relation in the following way:

$$\log_{10}(L_{144}) = a \log_{10}(\text{SFR}) + b, \quad (3)$$

where  $L_{144}$  is the spectral luminosity at 144 MHz in units of  $\text{W Hz}^{-1}$  and SFR is the star-formation rate in units of  $\text{M}_\odot \text{yr}^{-1}$ .

Therefore, first, we investigate the global radio continuum luminosities at 144 MHz as function of the SFR. The resulting relation is presented in Fig. 1. The data points fitted include only the global measurements, but for comparison we also show the local measurements. We find a best-fitting power-law as described Equation (3) with  $a = 1.48 \pm 0.07$  with a RMS data scatter of  $\sigma_y = 0.44$  dex (see Table 1 for the results this and the other fits to the global data presented in this work). We recall that for the global relation we find  $a = 1.4\text{--}1.5$  (Heesen et al. 2022), meaning a strong super-linear relation. In contrast, for the local relation we find  $a = 0.6\text{--}0.8$ , meaning a strong sub-linear relation (Heesen et al. 2024). Therefore, we do not expect that we can fit both data sets simultaneously. Still, fitting both global and local data together results in a large scatter of  $\sigma_y = 0.67$  dex.

We now compare our spatially resolved measurements with the global relation. These are shown as the small data points in Fig. 1. These points lie all on the left side of the plot at low values of the SFR. As can be seen clearly, they do not fit to the global relation, but mostly lie above it. The deviation is a strong function

Table 1: Best-fitting global relations using the equation  $\log_{10}(y) = a \log_{10}(x) + b$  for  $y = L_{144}$  or  $y = a \log_{10}(x) + b$  for  $y = \alpha$ . The variable  $\rho$  denotes Spearman’s correlation coefficient.

$y$	$a$	$b$	$x$	$\rho$
$L_{144}$	$1.480 \pm 0.070$	$21.957 \pm 0.057$	SFR	0.90
$L_{144}$	$1.180 \pm 0.051$	$21.57 \pm 0.048$	SFR <sub>TIR</sub>	0.93
$\alpha$	$-0.131 \pm 0.015$	$0.76 \pm 0.15$	$M_{\star}$	-0.68
$\alpha$	$0.132 \pm 0.019$	$-0.590 \pm 0.014$	SFR	-0.55
$\alpha$	$0.107 \pm 0.016$	$-0.553 \pm 0.014$	SFR <sub>TIR</sub>	-0.55
$\alpha$	$-0.28 \pm 0.03$	$-0.28 \pm 0.03$	$r_{\star}$	-0.70
$\alpha$	$-0.420 \pm 0.045$	$0.34 \pm 0.10$	$v_{\text{tot}}$	-0.67
$\alpha$	$0.023 \pm 0.014$	$-0.416 \pm 0.089$	$\Sigma_{\text{SFR}}$	0.24
$\alpha$	$0.006 \pm 0.016$	$-0.53 \pm 0.09$	$\Sigma_{\text{SFR,TIR}}$	0.15

of radio spectral index with data points with a steep spectrum lying furthest above the relation. Mostly, only data points with a radio spectral index indicative of a flat spectrum are in agreement with the global relation; although, even they may deviate significantly from it (in particular those at the lower-left end of the distribution). This behaviour has been interpreted in the literature as a result of cosmic-ray transport such as diffusion (Heesen et al. 2023). In our previous work we argued that energy-independent diffusion describes the data best (Heesen et al. 2024). Aside from cosmic-ray transport there may be influences of bursty star formation which can increase the scatter in the radio-SFR relation due to the different time-scales involved and the reliability of SFR estimates (Haskell et al. 2023). On the other hand, one may expect H II regions to lie below the global relation since radio emission is absorbed and CRE quickly escape these regions. We do not see such data points, possibly this can only be observed at frequencies below 100 MHz (Gajović et al. 2025).

### 3.2. Radio-to-SFR ratio

In this section, we investigate the origin of the radio-to-SFR ratio, which is defined as the ratio of radio continuum luminosity to the SFR. As shown in Sect. 3.1, the radio-to-SFR ratio depends on the radio spectral index. This is shown quite clearly in Fig. 2. We find that galaxies that are fairly radio bright in comparison to their SFR, have a steep radio continuum spectrum. The opposite is true for those galaxies with a flat spectrum. This trend can be observed for the global and the local measurements. The interesting question was whether both measurements follow the same trend. This is approximately the case, although the global measurements have slightly lower ratios than the local measurements at the same radio spectral index. Nevertheless, the agreement is in general quite good.

Hence, the parametrisation of the radio-to-SFR ratio with radio spectral index using both global and local data is as follows:

$$\log_{10}(L_{144}) - \log_{10}(\text{SFR}) = (-3.15 \pm 0.05)\alpha + (19.94 \pm 0.03), \quad (4)$$

using again the odr method. This result includes both the global and local data. The relation is slightly steeper than the one using only local data (Heesen et al. 2024).

### 3.3. Fundamental plane of the radio–SFR relation

Our results presented in Sect. 3.2 show a strong correlation between radio-to-SFR ratio and radio spectral index. In our previous work in Heesen et al. (2024) we had introduced a parametri-

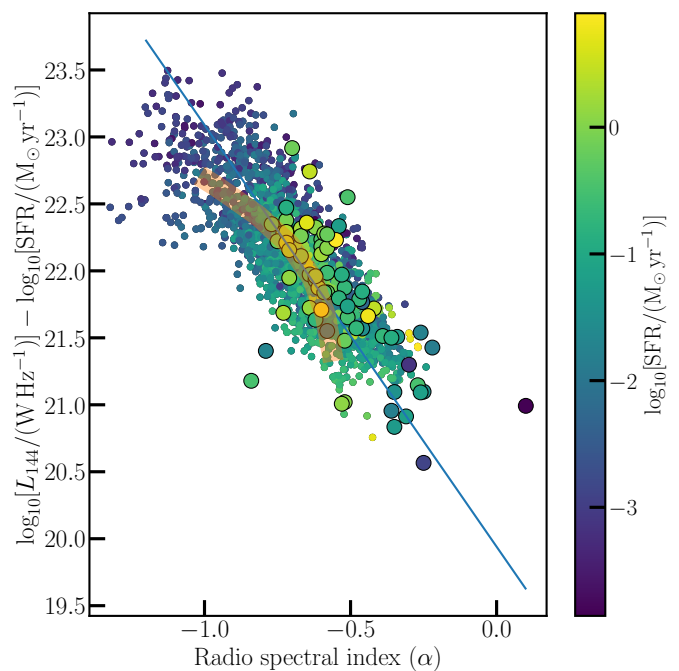


Fig. 2: Radio-to-SFR ratio as function of radio spectral index. We show the ratio of radio continuum luminosity to the SFR as function of radio spectral index. Large data points show global measurements and small data points local measurements. The blue line shows the best-fitting relation. The orange shaded thick line shows a model for a semi-calorimetric galaxy with cosmic-ray electrons radiation losses (see Sect 4.1).

sation where we correct the radio luminosity using Eq. (4). However, the more general parametrisation is as follows:

$$\log_{10}(L_{144}) = a \log_{10}(\text{SFR}) + b\alpha + c, \quad (5)$$

where  $a$ ,  $b$ , and  $c$  are constants. The only difference to Eq. (4) is that the slope of the radio-SFR relation as function of SFR is now the free parameter  $a$ ; previously we assumed the slope to be unity ( $a = 1$ ). We performed a bivariate least-squares fitting of our data with Eq. (5) including both binned local and global measurements. Our best-fitting parameters are  $a = 1.10 \pm 0.06$ ,  $b = -1.75 \pm 0.29$ , and  $c = 20.90 \pm 0.18$ . We found a standard deviation (scatter of data points around the best-fitting model) of 0.38 dex. This standard deviation is the lowest when compared with the other two-dimensional projections. For  $L_{144}$ –SFR we found 0.59 dex; SFR– $\alpha$  has a standard deviation of 1.09 dex and  $L_{144}$ – $\alpha$  has one of 1.23 dex. It is obvious that only a comparison with  $L_{144}$ –SFR is necessary when considering that it is the only strong correlation with a Spearman’s correlation coefficient of  $\rho = 0.93$  whereas the other correlations have  $|\rho| \leq 0.3$ .

Hence, we find that the radio luminosity is correlated with both SFR and the radio spectral index  $\alpha$ , at a highly significant level. In particular, we show for the first time that the data points define a ‘Fundamental Plane’ in the  $[\log(L_{144}), \log(\text{SFR}), \alpha]$  space. This is shown in Fig. 3 where we present a three-dimensional representation of these parameters. We have chosen a view point such that we looking onto the plane at an angle such that the top part is closer to us (with flat radio spectrum in yellow-green colour) than the bottom rear part (with a steep radio spectrum with a dark blue colour). In general, however, the data points lie in a plane. We note that the two-dimensional projection

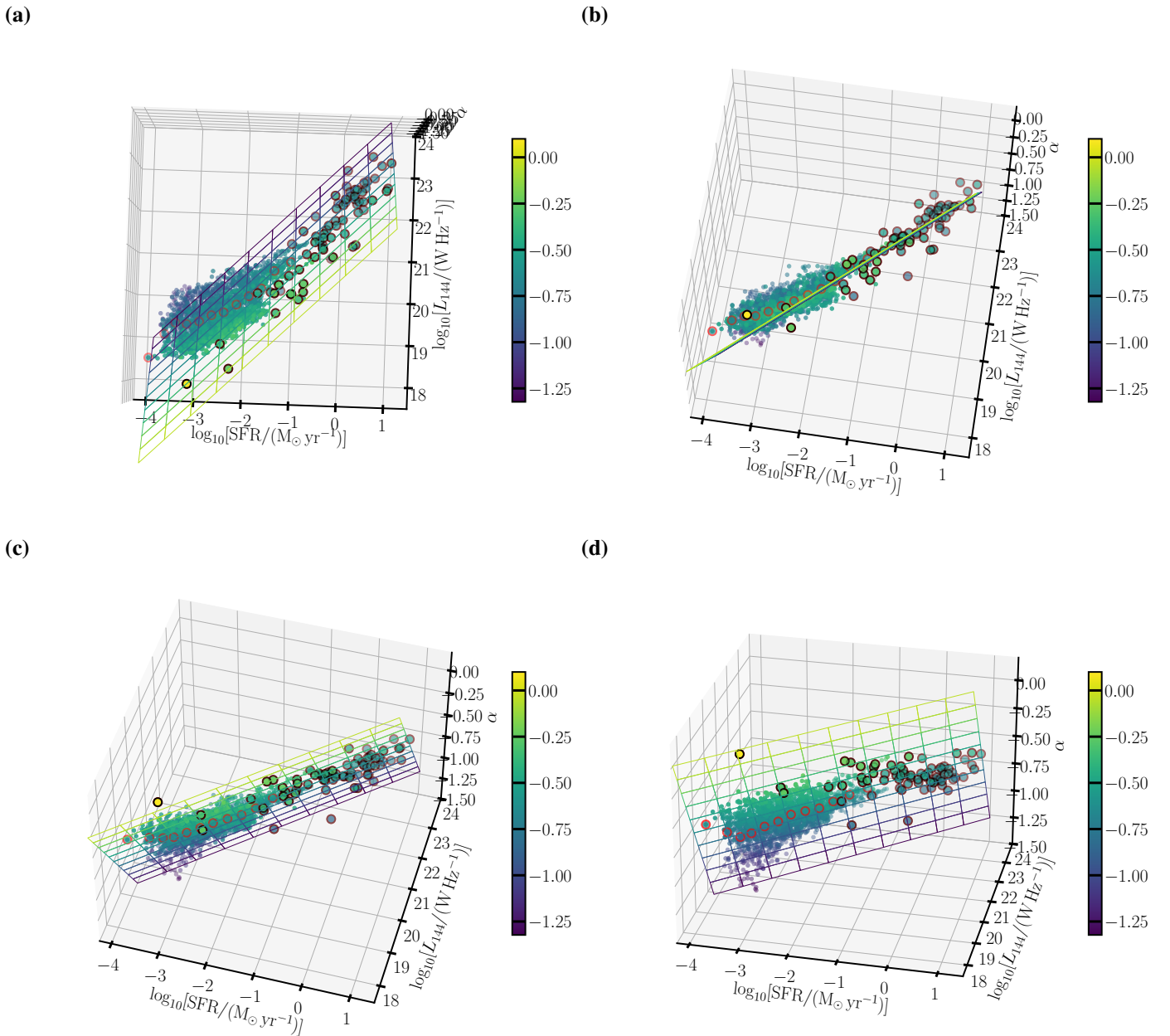


Fig. 3: Fundamental plane of the radio-SFR relation. The grid indicates the position of the fundamental plane; it shows the radio continuum luminosity for an equidistant set of lines in the  $[\log(\text{SFR}), \alpha]$  space with the colour coded with radio spectral index. Large data points with black boundaries show global measurements (individual galaxies) and small data points show local measurements. The colour of the data points is coded with the radio spectral index as indicated by the colour bar. Panel (a) shows the top view equivalent to the traditional radio-SFR relation (cf. Fig. 1); panel (b) shows the edge-on representation; panels (c) and (d) show different viewing angles with a perspective from the other side of the plane. An interactive version of this figure can be found [here](#).

in the  $\log(\text{SFR})$ – $\log(L_{144})$  plane is the radio-SFR correlation as presented in Fig 1.

There are only a few non-detected galaxies in the sample, but theoretically this could distort the results somewhat since we bias towards galaxies with high radio luminosities at low SFRs. The bias would result in somewhat smaller slopes of the radio-SFR relation as function of SFR. However, because their number (six) is so small, we expect the influence of this bias to be rather small.

### 3.4. Unified radio-SFR relation

The three-dimensional representation of the radio-SFR relation in the fundamental plane, allows us to define a unified relation that works both for global and local data. To this end we can choose a best-fit plane on which the most of the data lie.

This is shown in Fig. 4. On the y-axis, the radio continuum luminosity is divided by a correction factor using the radio spectral index. This can be done by re-writing Eq.(5):

$$\log_{10}(L_{144}) - b\alpha = a \log_{10}(\text{SFR}) + c. \quad (6)$$

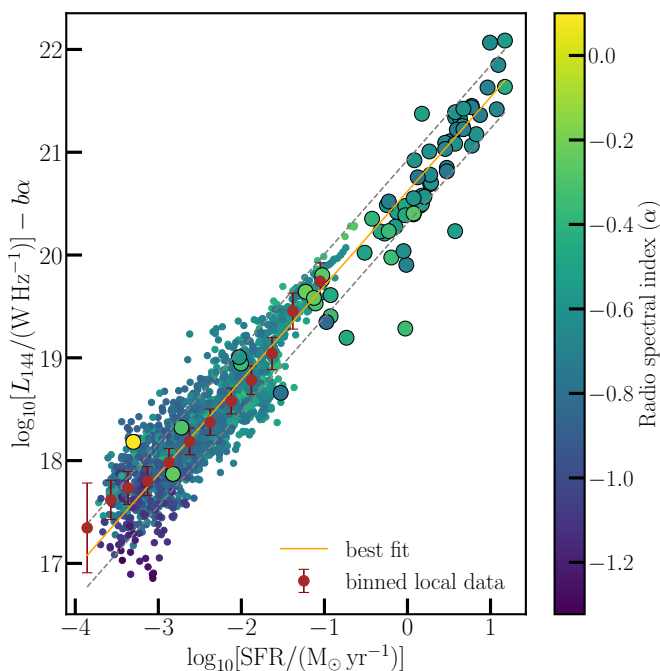


Fig. 4: Unified radio-SFR relation. We show the edge-on projection of the fundamental plane of the radio-SFR relation. The y-axis shows the radio continuum luminosity corrected for the radio spectral index,  $\log(L_{144}) - b\alpha$  (cf. Eq. 6), and the x-axis the SFR. Large data points with black boundaries show global measurements, large data points with red boundaries binned local measurements, and small data points local measurements. The best-fitting relation together with the  $\pm 1\sigma_y$  interval are shown as well. To be compared with Fig. 1.

Now plotting the left-hand side of Eq. (6) as function of the SFR, we would expect in the ideal case a unified radio-SFR relation where, both, local and global measurements follow the same trend. This is indeed at least approximately the case. The relation is slightly super-linear where global and local measurements now line up quite nicely. Comparing Fig. 1 with Fig. 4, the improvement is remarkable, in particular the agreement of local and global measurements. This means that we can reduce the scatter around the best-fitting relation by a significant amount using two frequencies instead of one, as we effectively do because we are using a two-point radio spectral index. Similar results were already found by Tabatabaei et al. (2017) at gigahertz frequencies for global measurements. The new aspect of our work is that this applies even to local (kiloparsec sized) measurements.

Figure 4 also shows that the trend of global data is not quite consistent. The global data could be fit with a slightly steeper linear relation than our combined fit. Consequently, the slope  $a$  in Eq. (5) depends on the binning of the local data. No binning results into sub-linear slopes. Whereas binning the local data as we did results in slightly super-linear slopes. Hence, we may want to keep in mind that the systematics of the binning may dominate the uncertainties of the best-fitting parameters of Eq. (5).

### 3.5. Influence of fundamental galaxy parameters

We now investigate the correlations of the global radio spectral index with fundamental galaxy parameters. Best-fitting correlations are presented in Table 1. We can see clear indications of correlations with SFR, stellar mass, size, and rotation velocity.

As an example, we present the correlation with stellar mass in Fig. 5. As found in our earlier work (Heesen et al. 2022), the radio continuum spectrum steepens with increasing mass of the galaxy. But, of course, the mass of the galaxy is highly correlated with SFR, size, and rotation speed. We find that the correlations are equally strong with the exception of the SFR where it is slightly weaker (as indicated by Spearman’s rank correlation coefficient). Similar results were found for a different sample of nearby galaxies by Grundy et al. (2025).

This correlation implies that galaxies with higher masses and higher SFRs have steeper radio continuum spectra. This can explain the super-linear radio-SFR slopes for global measurements. It is unknown which parameter determines the radio spectral index the most but the strongest correlations are with size, mass, and rotation speed. Notably, we find no correlation with the SFR surface density (as in Heesen et al. 2022). In Heesen et al. (2022) we presented a heuristic model that explains why size, and therefore in effect mass, may be the most important parameter while the SFR surface density plays no role. However, Smolinski et al. (2026) find a weak dependence on SFR surface density for the radio spectral index of the thick disc. Also, Tabatabaei et al. (2017) find such a correlation for the global spectral index at gigahertz frequencies. This may imply that other processes play a role at low frequencies, such as free-free absorption (Gajović et al. 2025) and cosmic ray ionisation losses (Gajović et al. 2024) that can flatten the spectrum.

On the other hand no such correlation is found for global measurements between radio spectral index and SFR surface density (Heesen et al. 2022, and this work). A correlation is found for gigahertz frequencies (Tabatabaei et al. 2017) or for the halo emission at low frequencies (Smolinski et al. 2026).

An important question is whether mass and spectral index are independent parameters for the radio-SFR correlation or whether they are related, and if so, which of the two parameters is more fundamental. We suggest that the spectral index is more fundamental because the radio power is immediately related to the spectral index, but only indirectly on mass. However, in the future one needs to check whether mass or any other fundamental galaxy parameter also spans another dimension. The assumption that massive galaxies are better calorimeters than low-mass galaxies is based on the assumption that the CR escape rate depends on mass. This is suggested by the fact that the radio continuum scale height has a negative correlation with mass surface density (Krause et al. 2018; Heesen et al. 2025). However, according to some simulations (e.g. Frommer et al. 2017) this is controversial and it is unclear whether CRs are passively driven by the baryonic wind, or whether the wind is driven by CRs. In the latter case, no mass dependence of the escape rate is expected and the magnetic field in the halo plays a role.

## 4. Discussion

### 4.1. Cosmic-ray electron calorimetry

Here, we investigate whether the strong dependence of the radio-to-SFR ratio on the radio spectral index (Sect. 3.2) can be explained within a simplified framework. Conceptually, when cosmic-ray electrons (CREs) escape freely from a galaxy, the observed spectral index equals the injection spectral index,  $\alpha_{\text{inj}}$ . Conversely, if the escape time-scale greatly exceeds the radiative loss time-scale (due to synchrotron and inverse-Compton cooling), the radio continuum spectrum steepens, and the spectral index decreases to  $\alpha_{\text{inj}} - 1$ . Hence, for an injection spectral index of  $\alpha_{\text{inj}} \approx -0.5$  we would expect a radio spectral index between

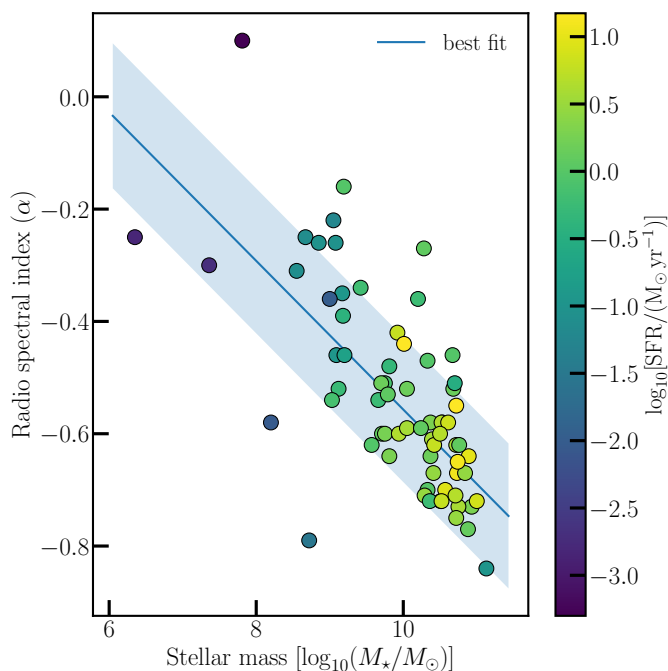


Fig. 5: Radio spectral index as a function of stellar mass. each data point is an individual galaxy. The blue line is the best-fitting relation and the shaded areas show  $\pm 1\sigma$ , RMS data scatter intervals. The data points are coloured according to their SFR values.

–1.0 and –0.5. At the same time, the radio continuum luminosity should decline as CRE escape becomes more efficient. The key question is thus how strongly this effect influences the observed radio emission.

To explore this, we constructed a simple model of CRE transport in a galactic wind designed to capture the essential physics of this process. Using the SPectral INdex Numerical Analysis of K(c)osmic-ray Electron Radio-emission (SPINNAKER; Heesen et al. 2016; Heald et al. 2022), we computed one-dimensional advection models of CRE transport that include only radiative energy losses from synchrotron and inverse-Compton processes. We assumed a galactic wind speed that is constant with  $100 \text{ km s}^{-1}$  and a disc magnetic field strength of  $B_0 = 8 \mu\text{G}$ . The halo magnetic field strength is then  $B = B_0 \exp(-z/h_B)$ , where  $h_B$  is the magnetic field scale height. Note that we used a fairly generic model that only attempts to reproduce the general features of escaping CRE and neglects the more complicated aspects of galactic winds. However, we do not expect that the details of the wind model to play an important role. Choosing a faster or slower wind speed could be compensated by a larger or smaller magnetic field scale height; accelerating galactic winds (e.g. Miskolczi et al. 2019; Heald et al. 2022) do also not significantly change this picture, as they only differ in that they include adiabatic losses that can be described by an energy-independent loss time-scale as the escape; finally, choosing a larger or smaller magnetic field strength can be compensated by a faster or smaller wind speed. Only, when the magnetic field strength would drop below  $\approx 3 \mu\text{G}$  we would expect a difference due to dominating inverse Compton losses in the radiation field of the cosmic microwave background. This would suppress the radio continuum luminosity. We then integrated the radio continuum luminosity along the line-of-sight to obtain the integrated intensity. This intensity is what we see when we look at the galaxy in projection. In the same way we calculated the radio spectral index. For the

CRE injection spectral index we choose  $p = 2.1$  resulting in  $\alpha_{\text{inj}} = -0.55$ . We varied the magnetic field scale height in order to model various degrees of CRE escape.

In Fig. 2 we show the resulting radio continuum intensities as a function of radio spectral index. We have varied only the magnetic field scale height using  $h_B = 2^n \times 0.75 \text{ kpc}$  with  $n = \{0, 1, \dots, 7\}$ . The model is able to reproduce the general features reasonably well, although there are some limitations at the extreme ends. When the radio spectral index is flat, close to the injection spectral index, the radio continuum intensity drops sharply, consistent with nearly free CRE escape. In contrast, as the radio spectral index approaches  $\alpha_{\text{inj}} - 0.5$ , in the limit of strong CRE radiation losses and no escape, the radio continuum luminosity increases. The model successfully explains the observed radio-to-SFR ratio for most spatially resolved data points; however, it underpredicts the ratio for regions with very flat spectra. Similarly, on global scales, galaxies exhibiting unusually flat spectra cannot be reproduced. This limitation arises because the model can only generate spectra approaching the injection slope, but not flatter ones, suggesting that additional physical processes must be at play in such systems. Examples for this are cosmic ray ionisation losses (e.g. Gajović et al. 2024) and free-free absorption (e.g. Adebahr et al. 2013; Gajović et al. 2025). Also, we note that we cannot distinguish between advection and energy-independent diffusion (Heesen et al. 2023).

#### 4.2. Radio-SFR relation parametrisation

In this section, we present several parametrisations of the radio-SFR relation. In particular, we are using our correlations of the radio spectral index together with the calorimetric efficiency. First we normalise our best-fitting relation to a radio spectral index of  $\alpha = -0.55$  which is close to the mean of our global data points which is  $\alpha = -0.54 \pm 0.17$ . This means:

$$\frac{L_{144}}{\text{W Hz}^{-1}} = 10^{21.87 \pm 0.18 - (1.72 \pm 0.29)(\alpha + 0.55)} \left( \frac{\text{SFR}}{\text{M}_{\odot} \text{ yr}^{-1}} \right)^{1.10 \pm 0.06} \quad (7)$$

This normalisation is in good agreement with previous measurements at the same frequency (Smith et al. 2021; Heesen et al. 2022). If the spectral index data are available, then Eq. (7) is the preferred way of estimating the SFR. However, since this is not generally the case, we present two more useful parametrisations of this general equation below. Entering the dependence of the radio spectral index on mass, we obtain:

$$\frac{L_{144}}{\text{W Hz}^{-1}} = 10^{21.87 \pm 0.18} \left( \frac{M_{\star}}{10^{10} \text{ M}_{\odot}} \right)^{0.23 \pm 0.05} \left( \frac{\text{SFR}}{\text{M}_{\odot} \text{ yr}^{-1}} \right)^{1.10 \pm 0.06} \quad (8)$$

This relation is in good agreement with the previously reported parametrisation of the radio-SFR relation with stellar mass (Shenoy et al. 2026). Finally, we can also express our relation only as function of SFR, when using the correlation between  $\alpha$  and SFR:

$$\frac{L_{144}}{\text{W Hz}^{-1}} = 10^{21.98 \pm 0.18} \left( \frac{\text{SFR}}{\text{M}_{\odot} \text{ yr}^{-1}} \right)^{1.33 \pm 0.08} \quad (9)$$

This last equation has a normalisation in good agreement with previous work. As expected from earlier works (e.g. Heesen et al. 2022), the relation is significantly super-linear.

## 5. Conclusions

We study nearby galaxies in LoTSS-DR3 (Shimwell et al. 2026), the third data release of the LoTSS (Shimwell et al. 2017, 2019, 2022). We included 70 galaxies, significantly expanding our previous sample from LoTSS-DR2 (Heesen et al. 2022). In particular, we included a few dwarf galaxies meaning that we expand the range of SFRs to now five orders of magnitude. We also included in our analysis the spatially resolved data at kiloparsec resolution that we previously analysed in Heesen et al. (2024). We measured radio continuum luminosities, SFRs, and radio spectral indices. We then investigated the correlations between radio continuum luminosity and SFR, the radio-SFR relation, and their dependence on radio spectral index. Finally, we consider the influence of other fundamental galaxy parameters. These are our main results:

1. For the first time, we show that the radio-SFR relation can be best described by a ‘fundamental plane’ which is defined in the  $(\log(L), \log(\text{SFR}), \alpha)$  space. With this description, the distinction between global and local relation vanishes and all data points fall on the same relation. The scatter of the data points around the best-fitting relation is improved from 0.67 dex to 0.38 dex.
2. Using an edge-on projection, correcting the radio continuum luminosity for the radio spectral index, we find a slightly super-linear relation with SFR. However, the slope depends on the weighting of global versus local data, with global data having a steeper trend.
3. The radio-to-SFR ratio, i.e. the ratio of radio continuum luminosity to SFR, has a strong dependence on radio spectral index. Galaxies that have steep radio continuum spectrum are brighter in the radio continuum at low frequencies. This can be in part explained by enhanced synchrotron losses of the CRE.
4. Galaxies with higher masses have steeper radio continuum spectra. With our observed dependence on the radio spectral index, we can therefore explain the reported mass dependence in the literature.

Our results show that it is possible to define a unified radio-SFR relation that hold both for global and local measurements. This unifies the previously reported super-linear relations for global measurements (e.g. Heesen et al. 2022) and the sub-linear relations for local measurements (e.g. Murphy et al. 2008; Heesen et al. 2024). The latter is ascribed to the influence of cosmic ray transport in a galaxy. Our results show the value of using a two-point radio spectrum rather than at a single frequency. This of course can be extended to even more frequencies (Tabatabaei et al. 2017; Grundy et al. 2025) in order to gain insights into the emission spectrum. In the future, it would be interesting to study the influence of the varying radio spectrum for instance at higher redshifts in order to better understand star formation rates in the early Universe.

Last but not least, great strides have been made to better understand the role of cosmic rays and magnetic fields in galaxy evolution (see e.g. Ruszkowski & Frommer 2023; Thompson & Heckman 2024, for recent reviews). The electron component of the cosmic rays can now be included with injection, transport, and various energy losses. Given the complexity of the physics involved, even the most advanced simulations have to make some simplifying assumptions. Thus, our results can serve as a simple of litmus test to test cosmological simulations with cosmic ray physics.

*Acknowledgements.* We thank the anonymous referee for a prompt and constructive report. We thank Rainer Beck and Dan Smith for valuable comments on the manuscript. MB acknowledges funding by the Deutsche Forschungsgemeinschaft (DFG) under Germany’s Excellence Strategy – EXC 2121 “Quantum Universe” – 390833306 and the DFG Research Group “Relativistic Jets”. MALL acknowledges grants PID2024-155875OB-I00 funded by MICIU/AEI/10.13039/501100011033/FEDER, EU and RYC2020-029354-I funded by MICIU/AEI/10.13039/501100011033 by “ESF Investing in your future”, by “ESF+”. LOFAR is the Low Frequency Array designed and constructed by AS-TRON. It has observing, data processing, and data storage facilities in several countries, which are owned by various parties (each with their own funding sources), and which are collectively operated by the LOFAR ERIC under a joint scientific policy. The LOFAR resources have benefited from the following recent major funding sources: CNRS-INSU, Observatoire de Paris and Université d’Orléans, France; BMFTR, MKW-NRW, MPG, Germany; Science Foundation Ireland (SFI), Department of Business, Enterprise and Innovation (DBEI), Ireland; NWO, The Netherlands; The Science and Technology Facilities Council, UK; Ministry of Science and Higher Education, Poland; The Istituto Nazionale di Astrofisica (INAF), Italy. This research made use of the Dutch national e-infrastructure with support of the SURF Cooperative (e-infra 180169) and the LOFAR e-infra group. The Jülich LOFAR Long Term Archive and the German LOFAR network are both coordinated and operated by the Jülich Supercomputing Centre (JSC), and computing resources on the supercomputer JUWELS at JSC were provided by the Gauss Centre for Supercomputing e.V. (grant CHTB00) through the John von Neumann Institute for Computing (NIC). This research made use of the University of Hertfordshire high-performance computing facility and the LOFAR-UK computing facility located at the University of Hertfordshire and supported by STFC [ST/P000096/1], and of the Italian LOFAR IT computing infrastructure supported and operated by INAF, and by the Physics Department of Turin university (under an agreement with Consorzio Interuniversitario per la Fisica Spaziale) at the C3S Supercomputing Centre, Italy. K.M. acknowledges the support of the Polish National Science Center (NCN) grant UMO-2024/53/B/ST9/00230. This research is part of the project LOFAR Data Valorization (LDV) [project numbers 2020.031, 2022.033, and 2024.047] of the research programme Computing Time on National Computer Facilities using SPIDER that is (co-)funded by the Dutch Research Council (NWO), hosted by SURF through the call for proposals of Computing Time on National Computer Facilities. This research made use of following software packages and other resources: Aladin sky atlas developed at CDS, Strasbourg Observatory, France (Bonnarel et al. 2000; Boch & Fernique 2014); ASTROPY (Astropy Collaboration et al. 2013, 2018); HyperLeda (<http://leda.univ-lyon1.fr>; Makarov et al. 2014); NASA/IPAC Extragalactic Database (NED), which is operated by the Jet Propulsion Laboratory, California Institute of Technology, under contract with the National Aeronautics and Space Administration; SAOImage DS9 (Joye & Mandel 2003); and SciPy (<https://scipy.org>; Virtanen et al. 2020).

## References

- Adebahr, B., Krause, M., Klein, U., et al. 2013, *A&A*, 555, A23  
 Astropy Collaboration, Price-Whelan, A. M., Sipőcz, B. M., et al. 2018, *AJ*, 156, 123  
 Astropy Collaboration, Robitaille, T. P., Tollerud, E. J., et al. 2013, *A&A*, 558, A33  
 Basu, A., Beck, R., Schmidt, P., & Roy, S. 2015, *MNRAS*, 449, 3879  
 Basu, A., Roy, S., & Mitra, D. 2012, *ApJ*, 756, 141  
 Belfiore, F., Leroy, A. K., Sun, J., et al. 2023, *A&A*, 670, A67  
 Bell, E. F. 2003, *ApJ*, 586, 794  
 Bendo, G. J., Galliano, F., & Madden, S. C. 2012, *MNRAS*, 423, 197  
 Boch, T. & Fernique, P. 2014, in *Astronomical Society of the Pacific Conference Series*, Vol. 485, *Astronomical Data Analysis Software and Systems XXIII*, ed. N. Manset & P. Forshay, 277  
 Bonnarel, F., Fernique, P., Bienaymé, O., et al. 2000, *A&AS*, 143, 33  
 Bosma, A., Goss, W. M., & Allen, R. J. 1981, *A&A*, 93, 106  
 Braun, R., Oosterloo, T. A., Morganti, R., Klein, U., & Beck, R. 2007, *A&A*, 461, 455  
 Brown, M. J. I., Moustakas, J., Kennicutt, R. C., et al. 2017, *ApJ*, 847, 136  
 Calzetti, D., Wu, S.-Y., Hong, S., et al. 2010, *ApJ*, 714, 1256  
 Chambers, K. C., Magnier, E. A., Metcalfe, N., et al. 2016, *arXiv e-prints*, arXiv:1612.05560  
 Condon, J. J., Cotton, W. D., Greisen, E. W., et al. 1998, *AJ*, 115, 1693  
 Crosthwaite, L. P., Turner, J. L., & Ho, P. T. P. 2000, *AJ*, 119, 1720  
 Dale, D. A., Bendo, G. J., Engelbracht, C. W., et al. 2005, *ApJ*, 633, 857  
 Dale, D. A., Cohen, S. A., Johnson, L. C., et al. 2009, *ApJ*, 703, 517  
 de Blok, W. J. G., Walter, F., Brinks, E., et al. 2008, *AJ*, 136, 2648  
 Dumas, G., Schinnerer, E., Tabatabaei, F. S., et al. 2011, *AJ*, 141, 41  
 Edler, H. W., de Gasperin, F., Shimwell, T. W., et al. 2023, *A&A*, 676, A24  
 Edler, H. W., Roberts, I. D., Boselli, A., et al. 2024, *A&A*, 683, A149

- Engelbracht, C. W., Gordon, K. D., Rieke, G. H., et al. 2005, *ApJ*, 628, L29
- Gajović, L., Adebahr, B., Basu, A., et al. 2024, *A&A*, 689, A68
- Gajović, L., Heesen, V., Brüggem, M., et al. 2025, *A&A*, 695, A41
- Gil de Paz, A., Boissier, S., Madore, B. F., et al. 2007, *ApJS*, 173, 185
- Grundy, J. A., Seymour, N., Wong, O. I., et al. 2025, *PASA*, 42, e002
- Gürkan, G., Hardcastle, M. J., Smith, D. J. B., et al. 2018, *MNRAS*, 475, 3010
- Hao, C.-N., Kennicutt, R. C., Johnson, B. D., et al. 2011, *ApJ*, 741, 124
- Haskell, P., Smith, D. J. B., Cochrane, R. K., Hayward, C. C., & Anglés-Alcázar, D. 2023, *MNRAS*, 525, 1535
- Heald, G. H., Heesen, V., Sridhar, S. S., et al. 2022, *MNRAS*, 509, 658
- Heesen, V. 2021, *Ap&SS*, 366, 117
- Heesen, V., Brinks, E., Leroy, A. K., et al. 2014, *AJ*, 147, 103
- Heesen, V., Buie, E. I., Huff, C. J., et al. 2019, *A&A*, 622, A8
- Heesen, V., Croston, J. H., Morganti, R., et al. 2018, *MNRAS*, 474, 5049
- Heesen, V., Dettmar, R.-J., Krause, M., Beck, R., & Stein, Y. 2016, *MNRAS*, 458, 332
- Heesen, V., Klocke, T. L., Brüggem, M., et al. 2023, *A&A*, 669, A8
- Heesen, V., Schulz, S., Brüggem, M., et al. 2024, *A&A*, 682, A83
- Heesen, V., Staffehl, M., Basu, A., et al. 2022, *A&A*, 664, A83
- Heesen, V., Stein, M., Pourjafari, N., et al. 2025, *A&A*, 699, A243
- Hindson, L., Kitchener, G., Brinks, E., et al. 2018, *The Astrophysical Journal Supplement Series*, 234, 29
- Irwin, J., Beck, R., Benjamin, R. A., et al. 2012, *AJ*, 144, 43
- Irwin, J., Beck, R., Cook, T., et al. 2024, *Galaxies*, 12, 22
- Jarrett, T. H., Masci, F., Tsai, C. W., et al. 2013, *AJ*, 145, 6
- Joye, W. A. & Mandel, E. 2003, in *Astronomical Society of the Pacific Conference Series*, Vol. 295, *Astronomical Data Analysis Software and Systems XII*, ed. H. E. Payne, R. I. Jedrzejewski, & R. N. Hook, 489
- Kamphuis, J. & Briggs, F. 1992, *A&A*, 253, 335
- Kapińska, A. D., Staveley-Smith, L., Crocker, R., et al. 2017, *ApJ*, 838, 68
- Kennicutt, Robert C., J., Armus, L., Bendo, G., et al. 2003, *PASP*, 115, 928
- Kennicutt, R. C., Calzetti, D., Aniano, G., et al. 2011, *PASP*, 123, 1347
- Kennicutt, R. C. & Evans, N. J. 2012, *ARA&A*, 50, 531
- Kennicutt, Jr., R. C., Hao, C.-N., Calzetti, D., et al. 2009, *ApJ*, 703, 1672
- Krause, M., Irwin, J., Wiegert, T., et al. 2018, *A&A*, 611, A72
- Lacki, B. C., Thompson, T. A., & Quataert, E. 2010, *ApJ*, 717, 1
- Lee, J. C., Gil de Paz, A., Kennicutt, Jr., R. C., et al. 2011, *ApJS*, 192, 6
- Leroy, A. K., Bigiel, F., de Blok, W. J. G., et al. 2012, *AJ*, 144, 3
- Leroy, A. K., Sandstrom, K. M., Lang, D., et al. 2019, *ApJS*, 244, 24
- Leroy, A. K., Walter, F., Brinks, E., et al. 2008, *AJ*, 136, 2782
- Li, J.-T., Beck, R., Dettmar, R.-J., et al. 2016, *MNRAS*, 456, 1723
- Makarov, D., Prugniel, P., Terekhova, N., Courtois, H., & Vauglin, I. 2014, *A&A*, 570, A13
- Miskolczi, A., Heesen, V., Horellou, C., et al. 2019, *A&A*, 622, A9
- Murphy, E. J., Condon, J. J., Schinnerer, E., et al. 2011, *ApJ*, 737, 67
- Murphy, E. J., Helou, G., Kenney, J. D. P., Armus, L., & Braun, R. 2008, *ApJ*, 678, 828
- Norris, R. P., Marvil, J., Collier, J. D., et al. 2021, *PASA*, 38, e046
- Pfrommer, C., Pakmor, R., Schaal, K., Simpson, C. M., & Springel, V. 2017, *MNRAS*, 465, 4500
- Rieke, G. H., Alonso-Herrero, A., Weiner, B. J., et al. 2009, *ApJ*, 692, 556
- Roth, M. A., Krumholz, M. R., Crocker, R. M., & Thompson, T. A. 2023, *MNRAS*, 523, 2608
- Ruszkowski, M. & Pfrommer, C. 2023, *A&A Rev.*, 31, 4
- Sanders, D. B., Mazzarella, J. M., Kim, D.-C., Surace, J. A., & Soifer, B. T. 2003, *AJ*, 126, 1607
- Shenoy, S., Smith, D. J. B., Biddle, S. K., et al. 2026, *MNRAS*[arXiv:2601.15374]
- Shimwell, T. W., Hardcastle, M. J., Tasse, C., et al. 2022, *A&A*, 659, A1
- Shimwell, T. W., Hardcastle, M. J., Tasse, C., et al. 2026, *A&A*, 707, A198
- Shimwell, T. W., Röttgering, H. J. A., Best, P. N., et al. 2017, *A&A*, 598, A104
- Shimwell, T. W., Tasse, C., Hardcastle, M. J., et al. 2019, *A&A*, 622, A1
- Smith, D. J. B., Haskell, P., Gürkan, G., et al. 2021, *A&A*, 648, A6
- Smolinski, D. C., Heesen, V., Brüggem, M., et al. 2026, *A&A*, 706, A374
- Tabatabaei, F. S., Krause, M., & Beck, R. 2007, *A&A*, 472, 785
- Tabatabaei, F. S., Schinnerer, E., Krause, M., et al. 2017, *ApJ*, 836, 185
- Thompson, T. A. & Heckman, T. M. 2024, *ARA&A*, 62, 529
- van Haarlem, M. P., Wise, M. W., Gunst, A. W., et al. 2013, *A&A*, 556, A2
- Vargas, C. J., Walterbos, R. A. M., Rand, R. J., et al. 2019, *ApJ*, 881, 26
- Virtanen, P., Gommers, R., Oliphant, T. E., et al. 2020, *Nature Methods*, 17, 261
- Werhahn, M., Pfrommer, C., & Girichidis, P. 2021, *MNRAS*, 508, 4072
- White, R. L. & Becker, R. H. 1992, *ApJS*, 79, 331
- Wiegert, T., Irwin, J., Miskolczi, A., et al. 2015, *AJ*, 150, 81
- Yun, M. S., Reddy, N. A., & Condon, J. J. 2001, *ApJ*, 554, 803

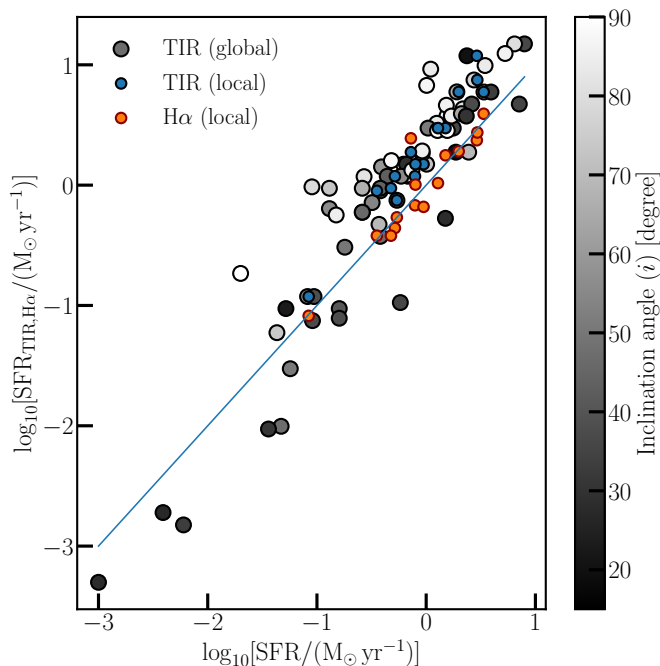


Fig. A.1: Comparison of SFRs. In this figure we compare the SFRs from the three different methods used. On the  $x$ -axis we show the SFRs as used in the main part of this work; for global data extinction-corrected  $H\alpha$  data and for local data extinction-corrected far-ultraviolet data. On the  $y$ -axis we show the SFRs for TIR and  $H\alpha$ . Global data are shown as large grey data points. Local data are shown as small blue (TIR) and orange ( $H\alpha$ ) data points. The 1:1 relation is shown as well as blue line.

## Appendix A: Observational results

In this section, we present observational and derived results for our sample galaxies. These include SFRs and radio continuum luminosities at 144 MHz, and radio spectral indices between 144 and approximately 1400 MHz. See Table A.1 for the compiled observational results of our sample.

### A.1. Star formation rates

We calculated SFRs with two different methods. The first method is to use dust-corrected  $H\alpha$  luminosities. The SFR is then calculated using the prescription from Kennicutt & Evans (2012). The resulting values are tabulated in Kennicutt et al. (2011). Again, for those galaxies where the values were not available, we calculated them ourselves. We used  $H\alpha$  fluxes and subtracted the contribution from  $N\text{II}$ . Then we used the  $24\ \mu\text{m}$  flux density to dust correct the  $H\alpha$  luminosity. For NGC 4125 we did not find a  $H\alpha$  flux, so we directly converted the mid-infrared luminosity into the SFR using the conversion from Rieke et al. (2009).

Second, we used the total infrared luminosity. The total infrared luminosity refers to a wavelength range of 3–1100  $\mu\text{m}$  using the values of Kennicutt et al. (2011), corrected to our distances. These values are based on *Herschel* measurements at 24, 70, and 160  $\mu\text{m}$  and using the prescription from Dale et al. (2009). For galaxies that are not part of the KINGFISH sample, we calculated the TIR luminosity using *IRAS* data at 25, 60, and 100  $\mu\text{m}$  using the prescription from Dale et al. (2009). The TIR luminosities are then converted into the SFRs using the conver-

sion from Kennicutt & Evans (2012), which is based on both Hao et al. (2011) and Murphy et al. (2011).

Detailed values with references used for calculating the SFRs for both methods can be found in Table A.2.

### A.2. Results with TIR SFRs

When using the TIR SFR values for the global data points, we obtain a smaller dependency on the SFR. When fitting Eq. (3) we obtain a slope of only  $1.18 \pm 0.05$ . The resulting figure is presented in Fig. A.2. The smaller power-law slope can be understood as a consequence of lower-mass systems. In them, the TIR luminosity underestimates the true SFR as they are low in dust content. Similarly, when fitting the fundamental plane (Eq. 5) we obtain  $a = 0.92 \pm 0.04$ ,  $b = -1.72 \pm 0.25$ , and  $c = 20.62 \pm 0.14$ . Again, the dependence on SFR is much smaller, in fact now even sub-linear. The corresponding unified radio-SFR relation is shown in Fig. A.3.

Finally, the ratio radio-to-SFR relation as function of radio spectral index becomes:

$$\log_{10}(L_{144}) - \log_{10}(\text{SFR}) = (-3.18 \pm 0.05)\alpha - (19.91 \pm 0.03), \quad (\text{A.1})$$

This relation is very similar to the results using the  $H\alpha$  and mid-infrared based SFRs. The reason is that the fit is dominated by the local data points that are identical.

### A.3. Comparison of SFRs

For our work we ideally would like to choose SFRs that are consistent for the entire sample, regardless whether this applies to global or local data. In principle, mid-infrared data is not a good star formation tracer in edge-on galaxies since the radiation becomes optically thick (e.g. Vargas et al. 2019). Therefore,  $H\alpha$  corrected luminosities underestimate the SFRs in highly inclined galaxies. This is shown in Fig. A.1, where one sees that highly inclined galaxies have larger TIR SFRs than obtained from  $H\alpha$ . On the other hand, at the lowest SFRs, the TIR-based SFRs are too low. The reason is that dwarf galaxies are low in dust and hence, some dust-heating photons escape the galaxy. Nevertheless, since we have many highly inclined galaxies in the sample from the CHANGE-ES survey, using would make sense from that perspective.

Now we look at the local SFRs. We now compare the sum of the local SFRs with the global SFRs in those 15 galaxies where we have local data. In the ideal case, they should agree. We do find, however, that the local SFRs are a factor of a few lower than the global SFRs in the same galaxies, if we use TIR-based global SFRs. This is shown as small blue data points in Fig. A.1. It is presently unclear why this deviation exists as these are not highly inclined galaxies. On the contrary, if we use  $H\alpha$ -based SFRs instead, we find a good agreement between local and global SFRs. This is shown as orange data points in Fig. A.1. Hence, on this basis we have chosen to use the SFRs from  $H\alpha$  for the global data points. In the next section (Sect. A.2), present alternative results when using TIR-based SFRs.

### A.4. Radio spectral indices

Radio spectral indices were calculated between 144 and approximately 1400 MHz. For this we used mostly published flux densities from the literature. See Table A.3 for details. In a few cases re-measured the flux densities from maps at the second frequency. For this we used the same integration ellipse as for the

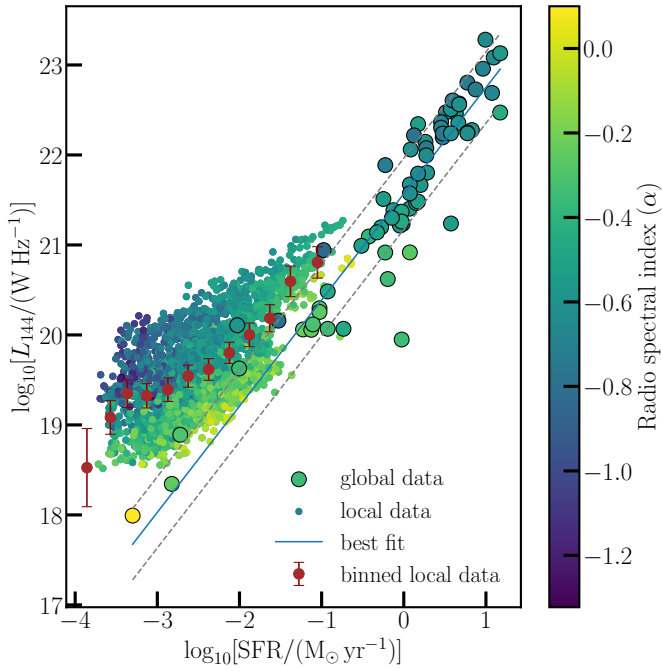


Fig. A.2: Radio-SFR relation. Same as Fig. 1 but using TIR-based SFR values.

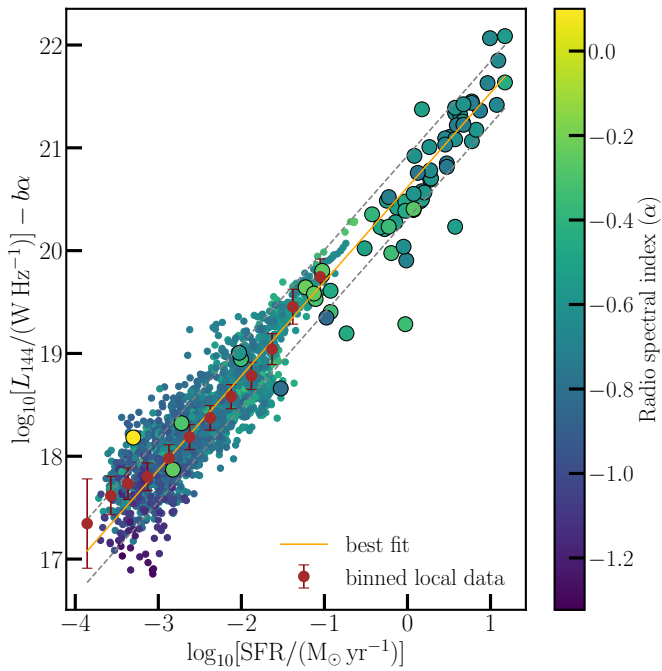


Fig. A.3: Unified radio-SFR relation. Same as Fig. 4 but using TIR-based SFR values.

LOFAR data. The major and minor semi-axes of these ellipses together with the position angle of the major axes can be found in Table A.1. We also used the projected semi-major axis as the distance of the galaxy to measure the star-forming radius  $r_*$ . With this the SFR surface density is calculated as  $\Sigma_{\text{SFR}} = \text{SFR}/(\pi r_*^2)$ . Rotation velocities with references can be found in Heesen et al. (2022).

Table A.1: Properties of galaxies in the sample.

Galaxy	$d$ (Mpc)	$\log_{10}(\text{SFR})$ ( $M_{\odot} \text{ yr}^{-1}$ )	$\log_{10}(\text{SFR}_{\text{TIR}})$ ( $M_{\odot} \text{ yr}^{-1}$ )	$\log_{10}(L_{144})$ (W Hz $^{-1}$ )	$\alpha$	$a_{20}$ ( $^{\circ}$ )	$b_{20}$ ( $^{\circ}$ )	$pa$ ( $^{\circ}$ )	$\log_{10}(M_{\star})$ ( $M_{\odot}$ )
(1)	(2)	(3)	(4)	(5)	(6)	(7)	(8)	(9)	(10)
IC 10	0.7	-1.33	-2.00	19.63 ± 0.04	-0.36 ± 0.04	5.0	4.0	129	9.00
NGC 598	0.9	-0.89	-0.19	20.62 ± 0.04	-0.34 ± 0.05	20.0	13.0	23	9.42
NGC 628	7.2	-0.17	0.07	21.67 ± 0.04	-0.59 ± 0.05	5.2	4.9	20	10.24
NGC 855	9.73	-1.37	-1.23	20.06 ± 0.04	-0.22 ± 0.09	0.7	0.6	67	9.05
NGC 891	9.1	0.19	0.57	22.51 ± 0.04	-0.62 ± 0.04	5.9	4.6	22	10.72
NGC 925	9.12	-0.27	-0.13	21.39 ± 0.04	-0.51 ± 0.06	5.6	3.1	287	9.75
IC 342	3.28	0.27	0.27	22.00 ± 0.04	-0.64 ± 0.09	17.0	12.0	37	9.81
NGC 2146	17.2	0.90	1.17	23.13 ± 0.04	-0.55 ± 0.04	2.6	2.4	123	10.72
NGC 2403	3.06	-0.42	-0.05	21.21 ± 0.04	-0.62 ± 0.06	11.1	5.1	124	9.57
Ho II	3.05	-1.44	-2.03	20.11 ± 0.04	-0.58 ± 0.05	3.0	2.5	15	8.20
DDO 53	3.61	-2.22	-2.82	18.34 ± 0.04	-0.25 ± 0.06	0.9	0.5	114	6.35
NGC 2683	6.27	-1.05	-0.01	21.23 ± 0.04	-0.70 ± 0.06	3.6	2.4	44	10.33
NGC 2798	25.8	0.53	0.77	22.25 ± 0.04	-0.42 ± 0.06	1.1	0.8	160	9.92
NGC 2820	26.5	-0.21	0.17	22.34 ± 0.04	-0.51 ± 0.04	3.2	1.2	65	9.70
NGC 2841	14.1	0.39	0.27	22.08 ± 0.04	-0.73 ± 0.05	3.9	2.9	153	10.93
NGC 2903	8.9	0.28	0.78	22.24 ± 0.04	-0.62 ± 0.05	5.1	4.1	204	10.42
Ho I	3.9	-2.41	-2.72	18.89 ± 0.04	-0.30 ± 0.10	2.0	1.0	50	7.36
NGC 2976	3.55	-1.09	-0.93	20.48 ± 0.04	-0.46 ± 0.05	3.0	2.8	143	9.09
NGC 3003	25.4	-0.17	0.08	22.06 ± 0.04	-0.60 ± 0.06	3.1	1.5	79	9.71
NGC 3031	3.44	-0.41	0.15	21.47 ± 0.04	-0.52 ± 0.05	11.7	5.9	330	10.68
NGC 3034	3.52	0.81	1.17	22.47 ± 0.04	-0.44 ± 0.05	6.2	7.0	66	10.01
NGC 3079	20.6	0.54	0.99	23.28 ± 0.04	-0.64 ± 0.04	3.9	2.3	167	10.89
NGC 3077	3.83	-1.03	-0.93	20.07 ± 0.04	-0.35 ± 0.06	1.4	1.2	49	9.17
M81 DwB	3.6	-3.00	-3.30	17.99 ± 0.04	0.10 ± 0.06	0.6	0.3	139	7.81
NGC 3184	11.7	-0.18	0.17	21.79 ± 0.04	-0.64 ± 0.05	4.1	4.1	179	10.37
NGC 3198	14.1	0.00	0.17	21.48 ± 0.04	-0.52 ± 0.07	3.4	1.5	215	10.05
IC 2574	3.79	-1.24	-1.53	20.16 ± 0.04	-0.79 ± 0.08	6.0	3.6	56	8.72
NGC 3265	19.6	-0.42	-0.43	21.09 ± 0.04	-0.39 ± 0.06	0.6	0.7	73	9.18
Mrk 33	15.4	0.18	-0.28	21.20 ± 0.04	-0.52 ± 0.07	0.8	0.7	129	9.12
NGC 3351	9.33	-0.23	0.07	20.92 ± 0.04	-0.27 ± 0.11	0.7	0.4	11	10.28
NGC 3432	9.42	-0.82	-0.25	21.51 ± 0.04	-0.54 ± 0.04	3.4	1.9	33	9.66
NGC 3448	24.5	-0.04	0.26	22.15 ± 0.04	-0.60 ± 0.04	1.8	1.2	65	9.75
NGC 3556	14.09	0.34	0.63	22.46 ± 0.04	-0.60 ± 0.04	4.4	3.2	79	9.94
NGC 3627	9.38	0.23	0.57	21.24 ± 0.04	-0.53 ± 0.05	4.2	3.1	173	10.67
NGC 3628	8.5	0.00	0.83	22.28 ± 0.04	-0.58 ± 0.05	6.9	3.4	104	10.61
NGC 3735	42.0	0.04	0.96	22.96 ± 0.04	-0.70 ± 0.04	2.3	1.5	130	10.57
NGC 3773	12.4	-0.80	-1.03	20.30 ± 0.04	-0.26 ± 0.06	0.6	0.6	161	8.85
NGC 3877	17.7	-0.04	0.28	21.80 ± 0.04	-0.58 ± 0.04	2.1	1.0	35	10.37
NGC 3938	17.9	0.25	0.47	22.20 ± 0.04	-0.71 ± 0.05	3.0	3.0	0	10.29
NGC 4013	16.0	-0.32	0.20	21.67 ± 0.04	-0.58 ± 0.04	2.1	0.9	65	10.53
NGC 4096	10.32	-0.57	0.07	21.40 ± 0.04	-0.53 ± 0.04	3.2	1.6	20	9.79
NGC 4125	24.77	-0.24	-0.98	20.94 ± 0.04	-0.84 ± 0.06	0.3	0.3	95	11.13
NGC 4157	15.6	0.10	0.51	22.47 ± 0.04	-0.72 ± 0.04	4.8	2.7	66	10.51
NGC 4214	2.95	-0.80	-1.11	20.12 ± 0.04	-0.31 ± 0.06	2.7	1.4	320	8.55
NGC 4217	20.6	0.18	0.66	22.36 ± 0.04	-0.58 ± 0.04	2.4	1.8	50	10.52
NGC 4236	4.45	-0.89	-0.03	19.95 ± 0.04	-0.35 ± 0.05	5.6	2.4	161	9.19
NGC 4244	4.4	-1.70	-0.73	20.07 ± 0.04	-0.46 ± 0.04	6.2	1.1	45	9.20
NGC 4254	14.4	0.59	0.77	22.80 ± 0.09	-0.72 ± 0.05	4.5	4.0	56	10.52
NGC 4321	14.3	0.42	0.67	22.57 ± 0.09	-0.71 ± 0.05	3.5	3.2	153	10.71
NGC 4449	4.02	-0.49	-0.14	21.30 ± 0.04	-0.54 ± 0.06	4.6	4.6	51	9.03
NGC 4450	14.07	-0.74	-0.52	20.99 ± 0.09	-0.51 ± 0.08	0.8	0.6	155	10.70
NGC 4559	6.98	-0.43	-0.33	21.14 ± 0.04	-0.48 ± 0.07	4.7	2.2	148	9.81
NGC 4565	11.9	-0.13	0.12	22.22 ± 0.04	-0.77 ± 0.04	8.0	2.5	135	10.88
NGC 4625	9.3	-1.28	-1.03	20.26 ± 0.04	-0.26 ± 0.15	0.9	0.7	330	9.08
NGC 4631	7.62	0.23	0.57	22.51 ± 0.04	-0.59 ± 0.04	8.8	7.5	86	10.05
NGC 4725	11.9	-0.36	0.07	21.57 ± 0.04	-0.62 ± 0.06	3.8	2.4	36	10.76
NGC 4736	4.66	-0.42	-0.03	21.37 ± 0.04	-0.47 ± 0.05	3.6	2.9	105	10.33
NGC 4826	5.27	-0.59	-0.23	20.92 ± 0.04	-0.36 ± 0.06	1.8	1.1	121	10.20
NGC 5033	17.13	0.03	0.59	22.61 ± 0.04	-0.73 ± 0.05	5.0	3.4	172	10.75

Table A.1: Properties of galaxies in the sample.

Galaxy	$d$ (Mpc)	$\log_{10}(\text{SFR})$ ( $M_{\odot} \text{ yr}^{-1}$ )	$\log_{10}(\text{SFR}_{\text{TIR}})$ ( $M_{\odot} \text{ yr}^{-1}$ )	$\log_{10}(L_{144})$ ( $\text{W Hz}^{-1}$ )	$\alpha$	$a_{20}$ ( $'$ )	$b_{20}$ ( $'$ )	$pa$ ( $^{\circ}$ )	$\log_{10}(M_{\star})$ ( $M_{\odot}$ )
(1)	(2)	(3)	(4)	(5)	(6)	(7)	(8)	(9)	(10)
NGC 5055	7.94	0.02	0.47	$22.24 \pm 0.04$	$-0.75 \pm 0.05$	6.6	4.9	102	10.72
NGC 5194	8.0	0.37	1.08	$22.69 \pm 0.04$	$-0.67 \pm 0.04$	6.9	6.7	195	10.73
NGC 5195	8.0	-0.59	-0.22	$21.89 \pm 0.04$	$-0.72 \pm 0.06$	2.0	1.8	79	10.36
NGC 5297	40.4	0.10	0.45	$22.36 \pm 0.04$	$-0.67 \pm 0.04$	2.5	1.2	147	10.41
NGC 5457	6.7	0.37	0.57	$22.24 \pm 0.04$	$-0.61 \pm 0.06$	11.3	11.3	39	10.39
NGC 5474	6.8	-1.04	-1.13	$20.06 \pm 0.04$	$-0.25 \pm 0.06$	2.2	1.6	100	8.67
NGC 5775	28.9	0.72	1.09	$23.08 \pm 0.04$	$-0.65 \pm 0.04$	2.9	1.8	148	10.74
NGC 5866	15.3	-0.59	-0.03	$21.26 \pm 0.04$	$-0.46 \pm 0.06$	1.0	0.6	127	10.67
NGC 5907	16.8	0.19	0.45	$22.30 \pm 0.04$	$-0.67 \pm 0.04$	5.8	2.0	156	10.84
NGC 6946	6.8	0.85	0.67	$22.56 \pm 0.04$	$-0.60 \pm 0.04$	7.3	6.4	243	10.50
NGC 7331	14.5	0.44	0.87	$22.73 \pm 0.04$	$-0.72 \pm 0.05$	5.4	2.8	168	11.00

**Notes.** Column (2)  $d$  is the distance (see Heesen et al. 2022, for references); (3) ; SFR from  $H\alpha$  and  $24 \mu\text{m}$  mid-infrared data (Sect. A.1); (4) SFR estimated from the TIR luminosity (Sect. A.1); (5) radio continuum luminosity at 144 MHz; (6) radio spectral index between 144 and approximately 1400 MHz (Sect. A.4); (7) semi-major axis of flux integration ellipse; (8) semi-minor axis of flux integration ellipse; (9) position angle of the semi-major axis of the integration ellipse (counting from North over East to South); (10) stellar mass (Leroy et al. 2019).

**References for position angles:** Hyperleda, except NGC 925, 2403, 2841, 2903, 3031, 3184, 3198, 3627, 4826, 5055, 6946, 7731, and IC 2574 (de Blok et al. 2008), NGC 628 (Kamphuis & Briggs 1992), IC 342 (Crosthwaite et al. 2000), NGC 3079, 3877, and 4157 (Krause et al. 2018), NGC 4214 and 4625 (Lee et al. 2011), NGC 5194 (Heesen 2021), NGC 5457 (Bosma et al. 1981), NGC 3938 (assumed to be zero), NGC 4254 and 4321 (this work).

Table A.2: Total infrared and dust-corrected H $\alpha$  luminosities for the galaxies in the sample.

Galaxy	$S_{25}$ (Jy)	$S_{60}$ (Jy)	$S_{100}$ (Jy)	$\log_{10}(L_{\text{TIR}})$ ( $L_{\odot}$ )	Ref.	$\log_{10}(F_{\text{H}\alpha+\text{NII}})$ ( $\text{erg s}^{-1} \text{cm}^{-2}$ )	$\text{N II}/\text{H}\alpha$	Ref.	$S_{24}$ (Jy)	Ref.	$\log_{10}(L_{\text{H}\alpha,\text{corr}})$ ( $L_{\odot}$ )
(1)	(2)	(3)	(4)	(5)	(6)	(7)	(8)	(9)	(10)	(11)	(12)
IC 10	4.00	31.00	71.00	7.82	I86	-9.91	0		9.81	B12	6.36
NGC 598				9.63	D05				50	E05	6.80
NGC 628				9.90	K11					K11	7.52
NGC 855				8.60	K11	-12.23	0.185	K09	0.082	D05	6.32
NGC 891	7.00	66.46	172.23	10.40	S03					V19	7.96
NGC 925				9.70	K11	-11.1	0.201	K09	0.9	D05	7.42
IC 342				10.10	K11					K11	7.96
NGC 2146				11.00	K11					K11	8.59
NGC 2403				9.78	D09	-10.25	0.088	K09	5.64	D05	7.27
Ho II				7.80	K11					K11	6.24
DDO 53				7.00	K11					K11	5.47
NGC 2683				9.81	D09					V19	7.08
NGC 2798				10.60	K11					K11	8.22
NGC 2820		3.00	10.00	10.00	M89					V19	7.82
NGC 2841				10.10	K11					K11	8.08
NGC 2903				10.60	D09					C10	7.97
Ho I				7.10	K11	-12.44	0.075	K09	0.013	D05	5.28
NGC 2976				8.90	K11	-11.19	0.357	K09	1.33	D05	6.60
NGC 3003		3.00	9.00	9.91	M86					V19	7.88
NGC 3031				9.98	D09	-10.32	0.545	K09	4.94	D05	7.28
NGC 3034				11.00	D09					C10	8.50
NGC 3079				10.82	E08					V19	8.39
NGC 3077				8.90	K11					K11	6.66
M81 DwB				6.50	K11					K11	4.69
NGC 3184				10.00	K11					K11	7.51
NGC 3198				10.00	K11					K11	7.69
IC 2574				8.30	K11	-11.23	0.046	K09	0.27	D05	6.44
NGC 3265				9.40	K11					K11	7.27
Mrk 33	1.00	5.00	5.00	9.55	M89					K11	7.86
NGC 3351				9.90	K11	-11.24	0.655	K09	2.4	D05	7.46
NGC 3432				9.58	D05					V19	7.39
NGC 3448	0.64	6.64	11.17	10.09	S03					V19	7.94
NGC 3556	4.19	32.55	76.90	10.46	S03					V19	8.24
NGC 3627				10.40	K11	-10.74	0.55	K09	7.25	D05	7.92
NGC 3628				10.66	D05					V19	7.84
NGC 3735	1.12	6.71	17.83	10.79	S03					V19	8.48
NGC 3773				8.80	K11	-11.99	0.233	K09	0.13	D05	6.89
NGC 3877	1.10	7.72	22.42	10.11	S03					V19	7.82
NGC 3938				10.30	K11					K11	7.94
NGC 4013	0.77	7.01	24.36	10.03	S03					V19	7.54
NGC 4096				9.90	D05					C10	7.54
NGC 4125		1.00	1.00	8.85	I86				0.069	D05	7.45
NGC 4157	2.12	17.71	50.67	10.34	S03					V19	7.93
NGC 4214	2.46	17.57	29.08	8.72	S03					H18	6.89
NGC 4217	1.50	11.60	41.19	10.49	S03					V19	7.96
NGC 4236				9.80	K11					K11	6.80
NGC 4244				9.09	D05					V19	6.47
NGC 4254				10.60	K11	-10.89	0.42	K09	4.09	D05	8.28
NGC 4321				10.50	K11	-11.06	0.43	K09	3.33	D05	8.10
NGC 4449				9.68	D05	-12.21	0.51	K09	0.19	D05	7.19
NGC 4450		1.00	7.00	9.31	I86					C10	6.94
NGC 4559				9.50	K11					K11	7.26
NGC 4565	1.36	7.79	34.62	9.95	S03					V19	7.67
NGC 4625				8.80	K11					K11	6.40
NGC 4631				10.40	K11					K11	7.92
NGC 4725				9.90	K11					K11	7.33
NGC 4736				9.80	K11					K11	7.27
NGC 4826				9.60	K11	-11.15	0.72	K09	2.47	D05	7.10
NGC 5033	2.14	16.20	50.23	10.42	S03	-11.23	0.48	K09	1.92	D05	7.71

Table A.2: Total infrared and dust-corrected H $\alpha$  luminosities for the galaxies in the sample.

Galaxy	$S_{25}$ (Jy)	$S_{60}$ (Jy)	$S_{100}$ (Jy)	$\log_{10}(L_{\text{TIR}})$ ( $L_{\odot}$ )	Ref.	$\log_{10}(F_{\text{H}\alpha+\text{NII}})$ ( $\text{erg s}^{-1} \text{cm}^{-2}$ )	N II/H $\alpha$	Ref.	$S_{24}$ (Jy)	Ref.	$\log_{10}(L_{\text{H}\alpha,\text{corr}})$ ( $L_{\odot}$ )
(1)	(2)	(3)	(4)	(5)	(6)	(7)	(8)	(9)	(10)	(11)	(12)
NGC 5055				10.30	K11	-10.8	0.486	K09	5.59	D05	7.70
NGC 5194				10.90	D05	-10.45	0.59	K09	12.25	D05	8.06
NGC 5195				9.60	D05				1.31	D05	7.10
NGC 5297		2.00	8.00	10.28	I86					V19	8.16
NGC 5457				10.40	K11					K11	8.05
NGC 5474				8.70	K11	-11.65	0.22	K09	0.18	D05	6.65
NGC 5775	2.47	23.59	55.64	10.92	S03					V19	8.57
NGC 5866				9.80	K11					K11	7.10
NGC 5907	1.44	9.14	37.46	10.28	S03					V19	8.03
NGC 6946				10.50	D05					K11	8.54
NGC 7331				10.70	D05					K11	8.12

**Notes.** Column (2)–(4) infrared flux density at 25, 60, and 100  $\mu\text{m}$ ; (5) total infrared luminosity at 2–1000  $\mu\text{m}$ ; (7) H $\alpha$  flux in  $\text{erg s}^{-1} \text{cm}^{-2}$ ; (8) fraction of NII; (10) flux density at 24  $\mu\text{m}$ ; (12) dust corrected H $\alpha$  flux

References: B12: [Bendo et al. \(2012\)](#); C10: [Calzetti et al. \(2010\)](#); D05: [Dale et al. \(2005\)](#); E05: [Engelbracht et al. \(2005\)](#); H19: [Hindson et al. \(2018\)](#); I86: IPAC 1986; K09: [Kennicutt et al. \(2009\)](#); K11: [Kennicutt et al. \(2011\)](#); S03: [Sanders et al. \(2003\)](#); V19: [Vargas et al. \(2019\)](#).

Table A.3: Radio spectral indices between 144 and approximately 1400 MHz.

Galaxy	$S_{144}$ (Jy)	$\nu$ (MHz)	$S_\nu$ (Jy)	$\alpha$	Ref.
IC 10	$0.721 \pm 0.072$	1580	$0.3060 \pm 0.0100$	$-0.36 \pm 0.04$	H18
NGC 598	$4.304 \pm 0.431$	1400	$1.9907 \pm 0.0995$	$-0.34 \pm 0.05$	T07
NGC 628	$0.756 \pm 0.076$	1365	$0.2000 \pm 0.0100$	$-0.59 \pm 0.05$	B07
NGC 855	$0.010 \pm 0.001$	1400	$0.0060 \pm 0.0010$	$-0.22 \pm 0.09$	NVSS
NGC 891	$3.294 \pm 0.329$	1575	$0.7432 \pm 0.0105$	$-0.62 \pm 0.04$	W15
NGC 925	$0.243 \pm 0.024$	1365	$0.0780 \pm 0.0080$	$-0.51 \pm 0.06$	B07
IC 342	$7.668 \pm 0.767$	1400	$1.8000 \pm 0.3000$	$-0.64 \pm 0.09$	T17
NGC 2146	$3.813 \pm 0.381$	1365	$1.1000 \pm 0.0100$	$-0.55 \pm 0.04$	B07
NGC 2403	$1.457 \pm 0.146$	1365	$0.3600 \pm 0.0300$	$-0.62 \pm 0.06$	B07
Ho II	$0.115 \pm 0.011$	1365	$0.0313 \pm 0.0016$	$-0.58 \pm 0.05$	B07
DDO 53	$0.001 \pm 0.000$	1400	$0.0008 \pm 0.0001$	$-0.25 \pm 0.06$	B17
NGC 2683	$0.362 \pm 0.036$	1575	$0.0680 \pm 0.0070$	$-0.70 \pm 0.06$	W15
NGC 2798	$0.222 \pm 0.022$	1400	$0.0860 \pm 0.0080$	$-0.42 \pm 0.06$	Y01
NGC 2820	$0.261 \pm 0.026$	1575	$0.0764 \pm 0.0012$	$-0.51 \pm 0.04$	W15
NGC 2841	$0.501 \pm 0.050$	1365	$0.0970 \pm 0.0070$	$-0.73 \pm 0.05$	B07
NGC 2903	$1.835 \pm 0.183$	1365	$0.4600 \pm 0.0100$	$-0.62 \pm 0.05$	B07
Ho I	$0.004 \pm 0.000$	4800	$0.0015 \pm 0.0005$	$-0.30 \pm 0.10$	T17
NGC 2976	$0.201 \pm 0.020$	1365	$0.0720 \pm 0.0050$	$-0.46 \pm 0.05$	B07
NGC 3003	$0.148 \pm 0.015$	1575	$0.0349 \pm 0.0041$	$-0.60 \pm 0.06$	W15
NGC 3031	$2.055 \pm 0.206$	1400	$0.6240 \pm 0.0312$	$-0.52 \pm 0.05$	W92
NGC 3034	$19.914 \pm 1.991$	1365	$7.4100 \pm 0.3700$	$-0.44 \pm 0.05$	A13
NGC 3079	$3.746 \pm 0.375$	1575	$0.8075 \pm 0.0162$	$-0.64 \pm 0.04$	W15
NGC 3077	$0.067 \pm 0.007$	1400	$0.0300 \pm 0.0030$	$-0.35 \pm 0.06$	Y01
M81DwB	$0.001 \pm 0.000$	1400	$0.0008 \pm 0.0001$	$0.10 \pm 0.06$	B17
NGC 3184	$0.377 \pm 0.038$	1365	$0.0890 \pm 0.0050$	$-0.64 \pm 0.05$	B07
NGC 3198	$0.127 \pm 0.013$	1365	$0.0390 \pm 0.0050$	$-0.52 \pm 0.07$	B07
IC 2574	$0.083 \pm 0.008$	1365	$0.0152 \pm 0.0020$	$-0.76 \pm 0.07$	B17
NGC 3265	$0.027 \pm 0.003$	1400	$0.0110 \pm 0.0010$	$-0.39 \pm 0.06$	Y01
Mrk 33	$0.055 \pm 0.006$	1400	$0.0170 \pm 0.0020$	$-0.52 \pm 0.07$	Y01
NGC3351	$0.079 \pm 0.008$	1400	$0.0430 \pm 0.0100$	$-0.27 \pm 0.11$	T17
NGC 3432	$0.304 \pm 0.030$	1575	$0.0833 \pm 0.0019$	$-0.54 \pm 0.04$	W15
NGC 3448	$0.195 \pm 0.019$	1575	$0.0465 \pm 0.0009$	$-0.60 \pm 0.04$	W15
NGC 3556	$1.215 \pm 0.122$	1575	$0.2909 \pm 0.0058$	$-0.60 \pm 0.04$	W15
NGC 3627	$1.636 \pm 0.164$	1365	$0.5000 \pm 0.0100$	$-0.53 \pm 0.05$	B07
NGC 3628	$2.177 \pm 0.218$	1365	$0.5900 \pm 0.0100$	$-0.58 \pm 0.05$	B07
NGC 3735	$0.429 \pm 0.043$	1575	$0.0813 \pm 0.0016$	$-0.70 \pm 0.04$	W15
NGC 3773	$0.011 \pm 0.001$	1400	$0.0060 \pm 0.0006$	$-0.26 \pm 0.06$	B17
NGC 3877	$0.169 \pm 0.017$	1575	$0.0423 \pm 0.0009$	$-0.58 \pm 0.04$	W15
NGC 3938	$0.409 \pm 0.041$	1365	$0.0820 \pm 0.0050$	$-0.71 \pm 0.05$	B07
NGC 4013	$0.151 \pm 0.015$	1575	$0.0378 \pm 0.0008$	$-0.58 \pm 0.04$	W15
NGC 4096	$0.198 \pm 0.020$	1575	$0.0560 \pm 0.0011$	$-0.53 \pm 0.04$	W15
NGC 4125	$0.012 \pm 0.001$	1365	$0.0018 \pm 0.0002$	$-0.84 \pm 0.06$	B07
NGC 4157	$1.021 \pm 0.102$	1575	$0.1845 \pm 0.0037$	$-0.72 \pm 0.04$	W15
NGC 4214	$0.126 \pm 0.013$	1400	$0.0620 \pm 0.0050$	$-0.31 \pm 0.06$	Y01
NGC 4217	$0.446 \pm 0.045$	1575	$0.1116 \pm 0.0022$	$-0.58 \pm 0.04$	W15
NGC 4236	$0.037 \pm 0.004$	1365	$0.0171 \pm 0.0009$	$-0.35 \pm 0.05$	B07
NGC 4244	$0.050 \pm 0.005$	1575	$0.0165 \pm 0.0006$	$-0.46 \pm 0.04$	W15
NGC 4254	$2.556 \pm 0.256$	1365	$0.4300 \pm 0.0215$	$-0.79 \pm 0.05$	B07
NGC 4321	$1.520 \pm 0.152$	1365	$0.3100 \pm 0.0100$	$-0.71 \pm 0.05$	B07
NGC 4449	$1.032 \pm 0.103$	1400	$0.3000 \pm 0.0300$	$-0.54 \pm 0.06$	NVSS
NGC 4450	$0.041 \pm 0.004$	1365	$0.0130 \pm 0.0020$	$-0.51 \pm 0.08$	B07
NGC 4559	$0.236 \pm 0.024$	1365	$0.0810 \pm 0.0100$	$-0.48 \pm 0.07$	B07
NGC 4565	$0.968 \pm 0.097$	1575	$0.1522 \pm 0.0030$	$-0.77 \pm 0.04$	W15
NGC 4631	$4.640 \pm 0.464$	1575	$1.1340 \pm 0.0370$	$-0.59 \pm 0.04$	W15
NGC 4725	$0.220 \pm 0.022$	1365	$0.0540 \pm 0.0050$	$-0.62 \pm 0.06$	B07
NGC 4736	$0.897 \pm 0.090$	1365	$0.3100 \pm 0.0200$	$-0.47 \pm 0.05$	B07
NGC 4826	$0.247 \pm 0.025$	1365	$0.1100 \pm 0.0100$	$-0.36 \pm 0.06$	B07
NGC 5033	$1.144 \pm 0.114$	1365	$0.2200 \pm 0.0100$	$-0.73 \pm 0.05$	B07

Table A.3: Radio spectral indices between 144 and approximately 1400 MHz.

Galaxy	$S_{144}$ (Jy)	$\nu$ (MHz)	$S_\nu$ (Jy)	$\alpha$	Ref.
NGC 5055	$2.286 \pm 0.229$	1365	$0.4200 \pm 0.0100$	$-0.75 \pm 0.05$	B07
NGC 5194	$6.363 \pm 0.636$	1365	$1.4100 \pm 0.0100$	$-0.67 \pm 0.04$	B07
NGC 5195	$1.004 \pm 0.100$	1365	$0.2000 \pm 0.0200$	$-0.72 \pm 0.06$	B07
NGC 5297	$0.118 \pm 0.012$	1575	$0.0238 \pm 0.0005$	$-0.67 \pm 0.04$	W15
NGC 5457	$3.226 \pm 0.323$	1400	$0.8080 \pm 0.0800$	$-0.61 \pm 0.06$	W92
NGC 5474	$0.021 \pm 0.002$	1400	$0.0120 \pm 0.0010$	$-0.25 \pm 0.06$	NVSS
NGC 5775	$1.212 \pm 0.121$	1575	$0.2550 \pm 0.0051$	$-0.65 \pm 0.04$	W15
NGC 5866	$0.065 \pm 0.006$	1400	$0.0230 \pm 0.0020$	$-0.46 \pm 0.06$	Y01
NGC 5907	$0.594 \pm 0.059$	1575	$0.1187 \pm 0.0036$	$-0.67 \pm 0.04$	W15
NGC 6946	$6.578 \pm 0.658$	1365	$1.7000 \pm 0.0100$	$-0.60 \pm 0.04$	B07
NGC 7331	$2.122 \pm 0.212$	1365	$0.4200 \pm 0.0200$	$-0.72 \pm 0.05$	B07

**Notes.** References: A13: [Adebahr et al. \(2013\)](#); B07: [Braun et al. \(2007\)](#); B17: [Brown et al. \(2017\)](#); H:18: [Heesen et al. \(2018\)](#); NVSS: integrated from NRAO Sky Survey maps ([Condon et al. 1998](#)); T07: [Tabatabaei et al. \(2007\)](#); T17: [Tabatabaei et al. \(2017\)](#); W15: [Wiegert et al. \(2015\)](#); W92: [White & Becker \(1992\)](#); Y01: [Yun et al. \(2001\)](#).